



Photometric Metallicity and Distance Estimates for $\sim 136,000$ RR Lyrae Stars from Gaia Data Release 3

Xin-Yi Li¹ , Yang Huang^{2,3,8} , Gao-Chao Liu⁴, Timothy C. Beers⁵ , and Hua-Wei Zhang^{6,7}

¹ South-Western Institute for Astronomy Research, Yunnan University, Kunming 650500, People's Republic of China

² School of Astronomy and Space Science, University of Chinese Academy of Sciences, Beijing 100049, People's Republic of China; huangyang@bao.ac.cn

³ National Astronomical Observatories, Chinese Academy of Sciences, Beijing 100101, People's Republic of China

⁴ Center for Astronomy and Space Sciences, China Three Gorges University, Yichang 443002, People's Republic of China

⁵ Department of Physics and Astronomy and JINA Center for the Evolution of the Elements, University of Notre Dame, Notre Dame, IN 46556, USA

⁶ Department of Astronomy, Peking University, Beijing 100871, People's Republic of China

⁷ Kavli Institute for Astronomy and Astrophysics, Peking University, Beijing 100871, People's Republic of China

Received 2022 June 29; revised 2022 December 19; accepted 2022 December 20; published 2023 February 14

Abstract

We present a sample of 135,873 RR Lyrae stars (RRLs) with precise photometric metallicity and distance estimates from our newly calibrated $P-\phi_{31}-R_{21}-[\text{Fe}/\text{H}]$ / $P-R_{21}-[\text{Fe}/\text{H}]$ and G -band absolute magnitude–metallicity relations. The $P-\phi_{31}-R_{21}-[\text{Fe}/\text{H}]$ and $P-R_{21}-[\text{Fe}/\text{H}]$ relations for type RRab and type RRc stars are obtained from nearly 2700 Gaia-identified RRLs, with precise ϕ_{31} and R_{21} measurements from light curves and metallicity estimates from spectroscopy. Using a few hundreds of nearby RRLs, with accurate distances estimated from the parallax measurements in Gaia Early Data Release 3, new G -band absolute magnitude–metallicity relations and near-IR period–absolute magnitude–metallicity relations are constructed. External checks, using other high-resolution spectroscopic samples of field RRLs and RRL members of globular clusters, show that the typical uncertainties in our photometric metallicity estimates are about 0.24 and 0.16 dex for type RRab and type RRc stars, respectively, without significant systematic bias with respect to the high-resolution spectroscopic metallicity measurements. The accuracies of these metallicity estimates are much improved, especially for type RRab stars, when compared to those provided by Gaia Data Release 3. Validations of our distance estimates, again using members of globular clusters, show that the typical distance errors are only 3%–4%. The distance moduli $\mu_0 = 18.503 \pm 0.001$ (stat) ± 0.040 (syst) mag for the Large Magellanic Cloud (LMC) and $\mu_0 = 19.030 \pm 0.003$ (stat) ± 0.043 (syst) mag for the Small Magellanic Cloud (SMC) are estimated from our type RRab star sample and are in excellent agreement with previous measurements. The mean metallicities of the LMC and SMC derived in this work are also consistent with previous determinations. Using our sample, a steep metallicity gradient of -0.024 ± 0.001 dex kpc^{-1} is found for the LMC, while a negligible metallicity gradient is obtained for the SMC.

Unified Astronomy Thesaurus concepts: RR Lyrae variable stars (1410); Distance indicators (394); Metallicity (1031); Magellanic Clouds (990)

Supporting material: machine-readable table

1. Introduction

RR Lyrae stars (RRLs) are old (>10 Gyr), low-mass ($<1 M_\odot$), metal-poor, periodic pulsating variable stars, which are mostly distributed in the bulge, thick disks, globular clusters (GCs), stellar halos, and substructures (e.g., dwarf galaxies and stellar streams) within the Galaxy. They are core helium-burning stars that are located on the horizontal branch on the Hertzsprung–Russell diagram, with relatively bright luminosities ($M_V \sim 0.65$ mag; e.g., Catelan & Cortés 2008; Muraveva et al. 2018a). According to their pulsating modes, RRLs can be divided into three types: RRab—fundamental-mode pulsating stars; RRc—first-overtone pulsating stars; and RRd—double-mode pulsating stars. They are ideal standard candles, thanks to their well-defined absolute magnitude–metallicity relations in the visual bands and period–absolute

magnitude–metallicity (PMZ) relations in the near/mid-IR bands. The above advantages of RRLs make them excellent tracers for probing the properties of our Galaxy, especially the stellar halo (Drake et al. 2013a; Iorio & Belokurov 2019, 2021; Wang et al. 2022b).

Over the years, many large-scale time-domain surveys have been conducted, and these have released large samples of RRLs, such as the Pan-STARRS1 survey (Sesar et al. 2017b), the Optical Gravitational Lensing Experiment (Soszyński et al. 2019), the Catalina survey (Drake et al. 2013b, 2014), the All-Sky Automated Survey for SuperNovae (Jayasinghe et al. 2019), and the Gaia Mission (Holl et al. 2018; Clementini et al. 2019, 2022).

Compared to photometric surveys, spectroscopic observations of RRLs are quite limited. Such spectra are particularly valuable, though, as they can provide vital measurements of RRLs—such as atmospheric parameters (effective temperature, T_{eff} , surface gravity, $\log g$, and metallicity, $[\text{Fe}/\text{H}]$) and line-of-sight velocities (v_{los})—to enable studies not only of the structure of the Milky Way, but also of the chemical and kinematic properties of our Galaxy. However, measurements of the stellar parameters for RRLs are quite challenging, since

⁸ Corresponding author.

they pulsate on short timescales (0.2–1.0 days) and their spectra can vary with time, even during a single exposure.

The most accurate way of determining the stellar parameters of RRLs is to use high-resolution spectra that have been observed at suitable phases (to avoid effects from shock waves; e.g., Fokin 1992; Pancino et al. 2015). But only a few hundred RRLs have been observed in this way (e.g., For et al. 2011; Kinman et al. 2012; Nemec et al. 2013; Govea et al. 2014; Pancino et al. 2015), due to the limited time available on large-aperture telescopes.

To obtain reliable metallicity estimates for a large sample of RRLs, Preston (1959) first proposed the ΔS index method, for low-resolution spectra that were observed at the phase of minimum light. Taking advantage of the massive low-resolution spectroscopic surveys, Liu et al. (2020; hereafter L20) presented the largest catalog to date, including more than 5000 RRLs with metallicity and v_{los} measurements, obtained with a template-matching method. The metallicities of RRLs can be accurately estimated down to about $[\text{Fe}/\text{H}] = -3.0$ using this method, with a typical uncertainty of 0.2 dex when compared to the results of high-resolution spectroscopy (HRS). This large catalog of RRLs is very powerful for studying the global properties and substructures of the Galactic stellar halo (Liu et al. 2022; Wang et al. 2022b).

Compared to the RRL samples from photometric surveys, RRLs with metallicity information built upon large-scale spectroscopic surveys also have significant shortcomings—e.g., shallower limiting magnitudes (thus smaller volumes being covered) and sparse sampling (thus suffering from potential selection effects). Given the pulsating nature of RRLs, their light curves are decided by a few physical parameters, including their chemical compositions. Observationally, such relations between the metallicity and the parameters yielded from decompositions of the light curves of RRab stars have been presented by Clement et al. (1992, 1993) and Kovacs & Zsoldos (1995). Subsequently, such relations have been applied in order to derive photometric metallicities for RRLs with precise light curve measurements (e.g., Jurcsik & Kovacs 1996; Smolec 2005; Morgan et al. 2007; Nemec et al. 2013; Ngeow et al. 2016; Hajdu et al. 2018; Dékány et al. 2021; Iorio & Belokurov 2021; Mullen et al. 2021, 2022; Dékány & Grebel 2022).

By using a few hundred local RRLs with very accurate light curves, and metallicities estimated from HRS, Nemec et al. (2013) presented very tight relations between $[\text{Fe}/\text{H}]$ and the parameters derived from light curves (i.e., the period and the Fourier decomposition parameter ϕ_{31}) for type RRab and type RRc stars, respectively, with scatters of about 0.1 dex. Most recently, Clementini et al. (2022; hereafter C22) released a large sample of 270,905 RRLs with full sky coverage, identified from the light curves obtained by Gaia Data Release 3 (DR3). By transforming the relations developed by Nemec et al. (2013) from the Kepler K_p band to the Gaia G band, C22 present metallicity estimates for 133,559 RRLs, with precise period and ϕ_{31} measurements from Gaia DR3. However, compared to the spectroscopic estimates, the metallicities derived by C22 have significant systematic bias and large uncertainties (especially for type RRab stars; see Section 3 for a detailed discussion).

In this study, by making use of ~ 2700 RRLs with precise metallicity estimates from L20, as well as period, ϕ_{31} , and R_{21}

measurements from the Gaia G band (C22), we calibrate the $P-\phi_{31}-R_{21}-[\text{Fe}/\text{H}]$ and $P-R_{21}-[\text{Fe}/\text{H}]$ relations⁹ for type RRab and type RRc stars in the Gaia G band directly. Using the metallicities estimated from the new relations for hundreds of local RRLs, with accurate distances estimated from parallax measurements, we further refine the G -band absolute magnitude–metallicity relations and the near-IR PMZ relations in the K_s and $W1$ bands for type RRab and type RRc stars, respectively.

This paper is organized as follows. In Section 2, we briefly describe the adopted data. In Section 3, we present the $P-\phi_{31}-R_{21}-[\text{Fe}/\text{H}]$ and $P-R_{21}-[\text{Fe}/\text{H}]$ relations as well as the $M_G-[\text{Fe}/\text{H}]$, $PM_{K_s}Z$, and $PM_{W1}Z$ relations for the RRLs, and derive the metallicities and distances for the full set of RRLs, with precise ϕ_{31} (and/or R_{21}) measurements that are based on the newly constructed relations. We present various checks on the derived photometric metallicities and distances in Section 4. In Section 5, we present the final RRL sample, as well as describe some potential applications of this catalog. Finally, a summary is presented in Section 6.

2. Data

2.1. Gaia RRL Sample

Based on the data released in Gaia DR3 (Gaia Collaboration et al. 2022), C22 have published 270,905 RRLs (including 174,947 stars of type RRab, 93,952 stars of type RRc, and 2006 stars of type RRd), processed by the dedicated Specific Objects Study (SOS) Cep&RRL pipeline (Clementini et al. 2019; Rimoldini et al. 2019). This pipeline provides estimates of the vital information for these RRLs, derived from the light curves of Gaia DR3, including the pulsation parameters (period, epoch of maximum light, peak-to-peak amplitudes, and intensity-averaged mean magnitudes for the Gaia G , G_{BP} , and G_{RP} bands) and the Fourier decomposition parameters (ϕ_{21} , ϕ_{31} , and R_{21}), from the G -band light curves. The SOS Cep&RRL pipeline also delivers radial velocity information for 1100 bright RRLs. The pulsation period, P , and the G -band amplitude are available for all 270,905 RRL candidates, and the ϕ_{31} and R_{31} Fourier decomposition parameters are available for 135,873 RRLs. In addition, the G -band absorption A_G for 142,660 type RRab stars is calculated from the G -band amplitude, pulsation period, and color, $G - G_{\text{RP}}$ (see C22 for details). They also estimate the photometric metallicities for 133,559 RRLs with available values of P and ϕ_{31} .

2.2. RRL Sample with Spectroscopic Metallicity Estimates

L20 have presented a large sample of metallicity estimates for 5290 RRLs. Their metallicities are estimated by matching more than 30,000 single-exposure low-to-medium-resolution spectra collected from the LAMOST (Deng et al. 2012; Zhao et al. 2012; Liu et al. 2014) and the SEGUE (Yanny et al. 2009) surveys to synthetic spectra. Various tests show that the typical

⁹ We note that C22 adopted the most often used $P-\phi_{31}-[\text{Fe}/\text{H}]$ relations for both type RRab and type RRc stars. However, the comprehensive analysis by Dékány et al. (2021) shows that the A_2 term from the Fourier decomposition is also tightly correlated with $[\text{Fe}/\text{H}]$, especially for type RRc stars, and that it is even more important than the contribution from P (see Figures 2 and 3 of Dékány et al. 2021). We thus adopt a $P-\phi_{31}-R_{21}-[\text{Fe}/\text{H}]$ relation for type RRab stars and a $P-R_{21}-[\text{Fe}/\text{H}]$ relation for type RRc stars (no significant improvement is obtained by adding the ϕ_{31} term). Here, we use R_{21} to represent A_2 , since no direct measurements of the latter are provided in the Gaia DR3 RRL catalog.

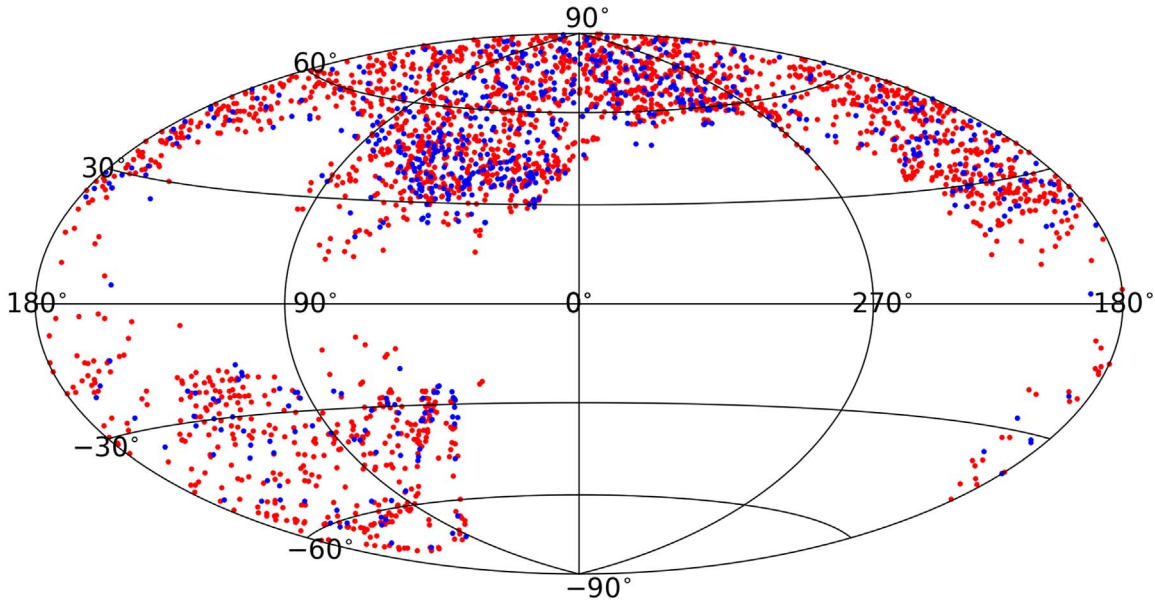


Figure 1. Sky distribution of our RRL_CAL_META sample of 2046 type RRab (red dots) and 641 type RRc (blue dots) stars, in Galactic coordinates.

uncertainty of the estimated metallicity is about 0.2 dex, without significant systematic offsets.

To calibrate the $P-\phi_{31}-R_{21}$ -[Fe/H] and $P-R_{21}$ -[Fe/H] relations for type RRab and type RRc stars (see the following section), the spectroscopic RRL sample of L20 is crossmatched with the photometric sample of C22, with the result that there are 2687 RRLs in common (2046 type RRab and 641 type RRc stars; hereafter, the RRL_CAL_META sample) after applying the following cuts: (1) spectral signal-to-noise ratios greater than 20; (2) measurement errors of [Fe/H] smaller than 0.2/0.15 dex for type RRab/RRc stars; (3) measurement errors of ϕ_{31} smaller than 0.5 for type RRab stars; (4) and measurement errors of R_{21} smaller than 0.15/0.05 for type RRab/RRc stars. Figure 1 presents the sky distribution of these stars.

3. Metallicity and Distance Estimates

In this section, we calibrate the $P-\phi_{31}-R_{21}$ -[Fe/H] and $P-R_{21}$ -[Fe/H] relations for type RRab and type RRc stars, respectively, by using the RRL_CAL_META sample described in the previous section. These relations are then applied for all the RRLs with precise measurements of P , ϕ_{31} , and R_{21} , to derive their metallicities. Moreover, by using about hundreds of local bright RRLs with accurate distances from Gaia parallax measurements and photometric metallicities, the M_G -[Fe/H] and PMZ relations for the RRLs are constructed. The newly derived M_G -[Fe/H] relations are then used to derive the distances of all RRLs with photometric metallicity estimates.

3.1. Metallicity

Before calibrating the new $P-\phi_{31}-R_{21}$ -[Fe/H] and $P-R_{21}$ -[Fe/H] relations, we compare the photometric metallicity estimates to those from C22, by using the RRL_CAL_META sample. The results are shown in Figure 2. For type RRab stars, the photometric metallicities from C22 are systematically higher than those from the spectroscopic estimates of L20, by 0.33 dex, plus there is a dispersion of 0.41 dex. For type RRc stars, the photometric metallicities

of C22 are slightly higher than those of L20, by 0.16 dex, with a scatter of 0.24 dex.

To improve the accuracies of the photometric metallicity estimates, we calibrate the $P-\phi_{31}-R_{21}$ -[Fe/H] and $P-R_{21}$ -[Fe/H] relations for type RRab and type RRc stars, respectively, using the RRL_CAL_META sample, as described above.

For type RRab stars, the relation is built by fitting data points to the linear model inspired by the comprehensive analysis of Dékány et al. (2021):

$$\begin{aligned} [\text{Fe}/\text{H}] = & a_0 + a_1(P - 0.6) + a_2(\phi_{31} - 2) \\ & + a_3(R_{21} - 0.45), \end{aligned} \quad (1)$$

where P is the period, ϕ_{31} and R_{21} are the Fourier parameters of the Gaia G -band light curve, [Fe/H] is the spectroscopic metallicity estimated by L20, and a_i ($i = 0, \dots, 3$) are the fit coefficients.

As shown in Figure 3, the metallicities of our RRL_CAL_META sample are not uniformly distributed, with most of the stars located between $[\text{Fe}/\text{H}] = -1.0$ and -2.0 , and a fewer stars outside this range, which can lead to biases in fitting the relation. Similar to Dékány & Grebel (2022), we have applied density-dependent sample weights to the fitting process. The weight (ω_d) of each star is calculated from the normalized Gaussian kernel density (ρ_d) of the metallicity distribution. We set ω_d to $0.6/\rho_d$ for $\rho_d \geq 0.15$, and to a constant value of 4, if $\rho_d < 0.15$. The latter threshold is introduced to avoid excessive influence from Poisson noise, due to there being fewer data points for deriving the density. 3σ clipping is also performed during the fitting process.

The resulting fit coefficients are listed in Table 1. A comparison between the spectroscopic metallicities $[\text{Fe}/\text{H}]_{\text{L20}}$ and our photometric $[\text{Fe}/\text{H}]_{\text{phot}}$ estimates is shown in the left panel of Figure 3. These estimates are quite consistent with one another, with an offset of -0.05 dex and a much improved scatter of 0.24 dex (compared to the result of C22; see the left panel of Figure 2). We note that a mild bias of around 0.3 dex is found at $[\text{Fe}/\text{H}]_{\text{phot}} \sim -2.9$, although large weights are assigned for metal-poor sample stars, as mentioned above.

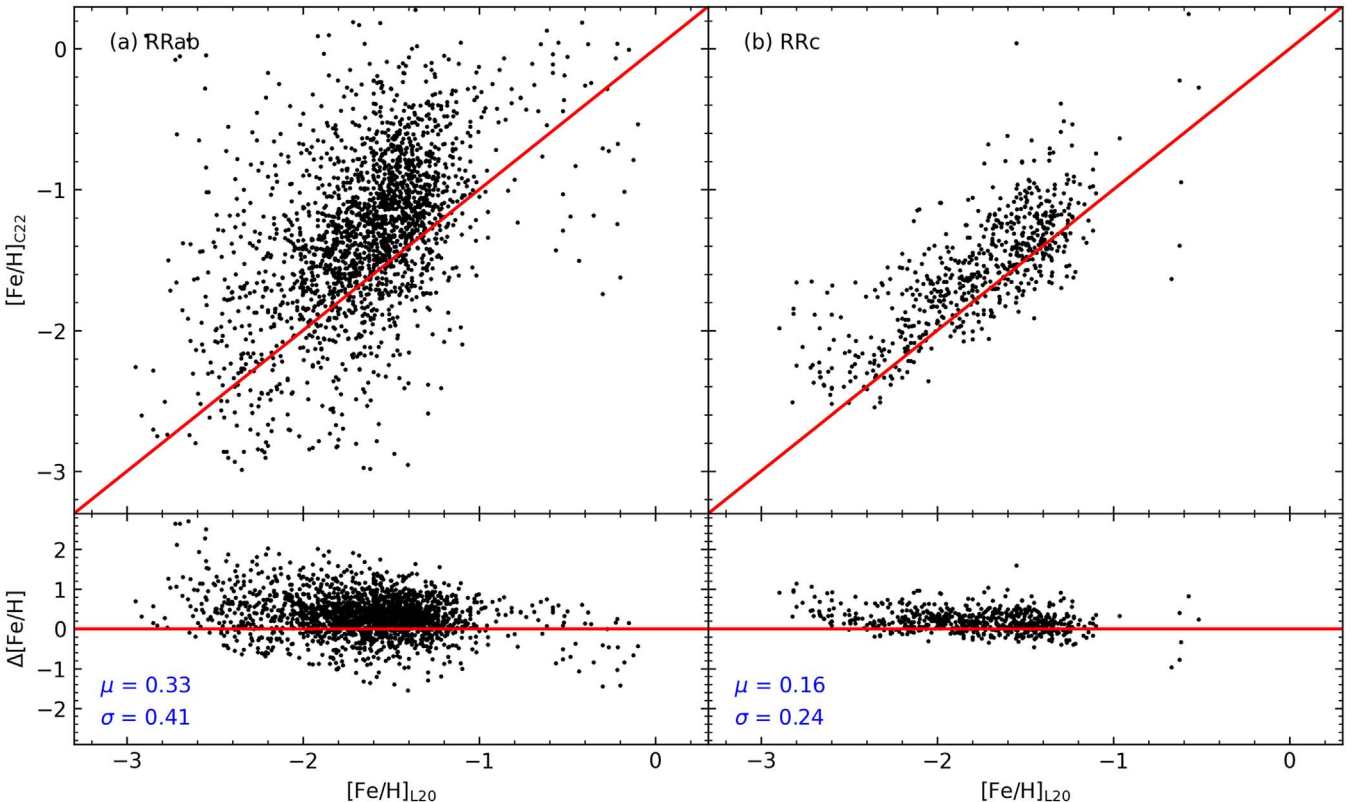


Figure 2. Comparison of the estimated photometric metallicities from C22, $[Fe/H]_{C22}$, with the spectroscopic metallicities from L20, $[Fe/H]_{L20}$, for 2069 type RRab and 641 type RRc stars, respectively. The differences in the metallicities, $\Delta[Fe/H]$ (in the sense of C22 minus L20), are shown in the lower parts of each panel, with the means and standard deviations marked in the bottom left corners.

This is a common issue for current calibrations, such as the efforts of Dékány et al. (2021) and Dékány & Grebel (2022), but it is expected that one will be able to reduce these systematics by assembling more metal-poor RRLs with precise metallicity measurements from HRS in the near future.

Inspired by the study of Dékány et al. (2021), again, a first-order 2D polynomial fitting is applied to the $[Fe/H]$ estimates for the type RRc stars from L20, as a function of their period and R_{21} from C22:

$$[Fe/H] = a_0 + a_1(P - 0.3) + a_2(R_{21} - 0.2), \quad (2)$$

where a_i ($i = 0, 1, 2$) are the fit coefficients. Again, density-dependent sample weights and 3σ clipping are performed in the fitting process. The fit coefficients are also listed in Table 1. The right panel of Figure 3 shows that the photometric metallicities resulting from Equation (2) are in excellent agreement with the spectroscopic ones, with an offset of -0.03 dex and a small scatter of 0.19 dex.

We caution that the above relations could be affected by the well-known Blažko effect, a phenomenon of amplitude and/or phase modulation with a quasi-period of tens to 100 days, first found by Blažko (1907). The origin of this phenomenon remains uncertain. Measurements of ϕ_{31} and R_{21} are affected for the RRLs suffering the Blažko effect, causing deviations of their $P-\phi_{31}-R_{21}-[Fe/H]$ and $P-R_{21}-[Fe/H]$ relations. As reported by previous studies (e.g., Smolec 2016; Netzel et al. 2018), the incidence rate of this effect for type RRab stars is much greater than that for type RRc stars. In addition, the uncertainty of the snapshot-derived spectroscopic metallicity (from L20) of type RRab stars is larger than that for type RRc

stars, due to the larger amplitudes of the former. These may explain why the $P-R_{21}-[Fe/H]$ relation of type RRc stars is much tighter than that for type RRab stars, as well as the presence of fewer outliers in the fits for type RRc stars than for type RRab stars (the red crosses in Figure 3).

The newly constructed relations are then applied to those RRLs with precise measurements of period, ϕ_{31} , and R_{21} from C22, to derive their photometric metallicities. In total, estimates of the metallicities for 135,873 RRLs (115,410 type RRab and 20,463 type RRc stars) are obtained for our final RRL sample. The uncertainties in the photometric metallicity estimates are primarily from two sources: errors in the period, ϕ_{31} , and R_{21} measurements and fit coefficient errors, as well as errors from the method itself. The former error can be estimated by a Monte Carlo (MC) simulation. For each star, 1000 MC simulations are performed, by sampling the measurement uncertainties of the period, ϕ_{31} , and R_{21} given by C22, and the errors of the fit coefficients in Table 1. The random error of each star is then estimated from the distribution yielded by the MC simulations. The latter errors are provided by the scatter in the fits described above (see also the lower sections of Figure 3).

The metallicity distribution of our final RRL sample is presented in Figure 4, while the distribution of the mean metallicity for this sample in Galactic coordinates is shown in Figure 5. This figure exhibits a negative gradient in metallicity from the Galactic plane toward high Galactic latitude, in agreement with our expectation. Moreover, the Large Magellanic cloud (LMC) and the Small Magellanic cloud (SMC) are clearly seen on the map.

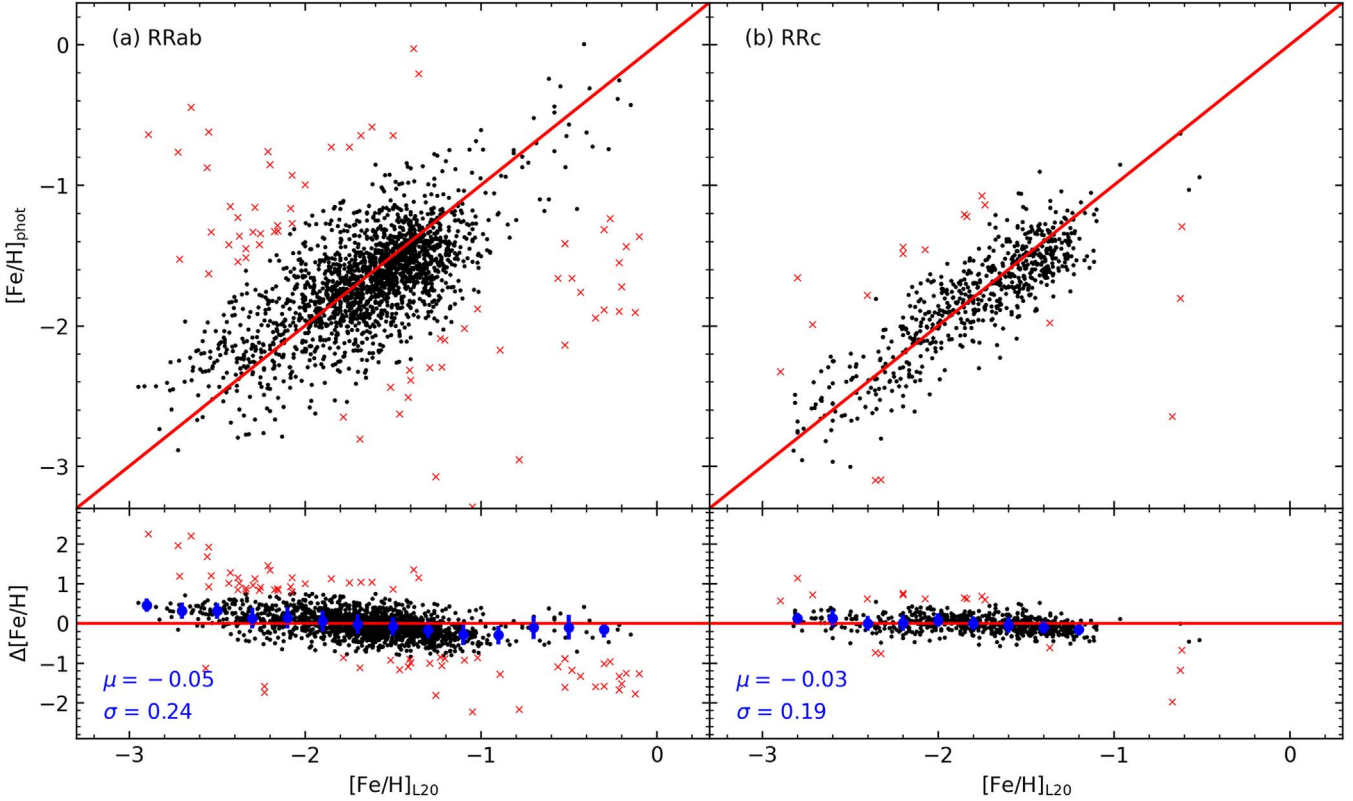


Figure 3. Left: the top panels show the spectroscopic and our photometric metallicities for 2046 type RRab stars in our RRL_CAL_META sample. Right: the same as the left panel, but for 641 type RRc stars in our RRL_CAL_META sample. In both panels, the red crosses show data points that are excluded by the 3σ clipping, while the black dots represent the data points that are adopted in the final fitting. The differences $\Delta[\text{Fe}/\text{H}]$ (in the sense of this work minus that of L20) are shown in the lower part of each panel, with the means and standard deviations marked in the bottom left corners. The blue dots and the associated error bars are the median values and standard deviations of $\Delta[\text{Fe}/\text{H}]$ in the individual $[\text{Fe}/\text{H}]_{\text{L20}}$ bins.

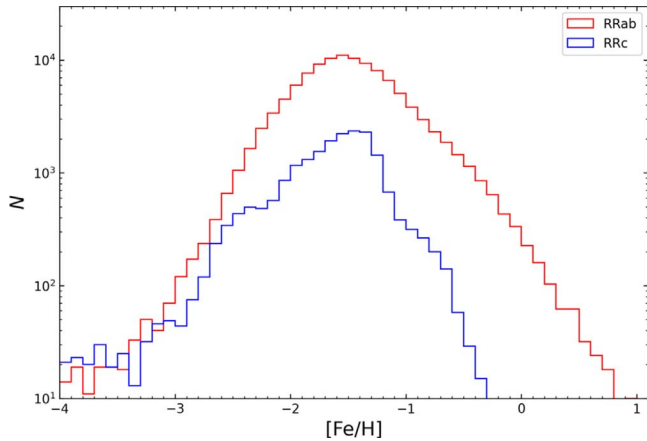


Figure 4. The photometric metallicity distributions of the type RRab (red line) and type RRc (blue line) stars in our final RRL sample.

3.2. Distance

The RRLs are well-behaved distance indicators, given the well-known absolute magnitude–metallicity relations (e.g., $M_G - [\text{Fe}/\text{H}]$) in the visual bands and the PMZ relation in the IR bands. Calibrations of these relations require a large sample of RRLs, with a wide metallicity distribution and accurate measurements of the absolute magnitudes. With a large sample of photometric metallicity estimates for RRLs, one can recalibrate the relations by selecting local bright RRLs that have photometric metallicity estimates given by this study and accurate distance measurements from the parallaxes reported in

Table 1
Fit Coefficients

Coeff.	$[\text{Fe}/\text{H}]_{\text{RRab}}^{\text{a}}$	$[\text{Fe}/\text{H}]_{\text{RRc}}^{\text{b}}$
a_0	-1.888 ± 0.002	-1.737 ± 0.005
a_1	-5.772 ± 0.026	-9.968 ± 0.079
a_2	1.090 ± 0.005	-5.041 ± 0.051
a_3	1.065 ± 0.030	...

Notes.

^a The fitting function is given by Equation (1).

^b The fitting function is given by Equation (2).

Gaia Early Data Release 3 (EDR3). We define the calibration sample by crossmatching our final RRL sample to Gaia EDR3, with the following cuts:

1. For type RRab stars, the value of $E(B - V)$ must be less than 0.1 mag, either from Schlegel et al. (1998; hereafter, SFD98),¹⁰ for high-latitude regions ($|b| \geq 25^\circ$), or from C22, for low-latitude regions ($|b| < 25^\circ$);
2. For type RRc stars, the value of $E(B - V)$ must be less than 0.2 mag, as given by SFD98 for high-latitude regions with $|b| \geq 20^\circ$;
3. The RRLs must have parallaxes greater than 0.25 mas and relative parallax errors smaller than 10%;

¹⁰ The values of $E(B - V)$ from SFD98 are corrected for a systematic of 14%, as reported in previous studies (e.g., Schlafly et al. 2010; Yuan et al. 2013).

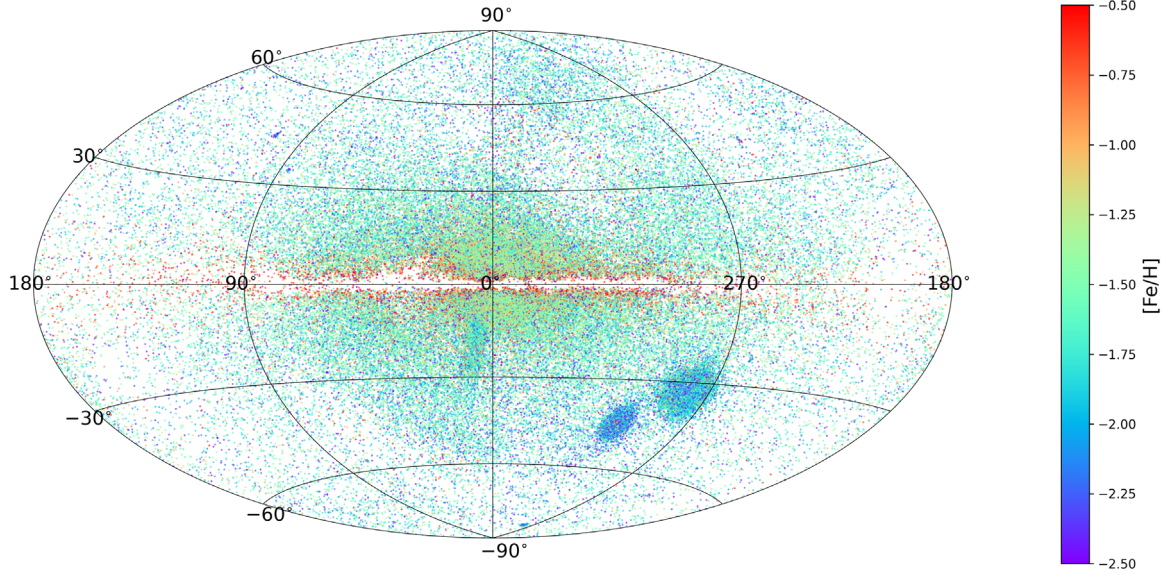


Figure 5. The sky distribution of our final RRL sample of 135,873 RRLs (115,410 type RRab and 20,463 type RRc stars) in Galactic coordinates, color-coded by metallicity, as shown in the color bar.

4. The errors of the photometric metallicities must be less than 0.3 and 0.2 dex for type RRab and RRc stars, respectively; and
5. The RRLs must have $\text{phot_bp_rp_excess_factor} < 1.5$ and $\text{astrometric excess noise} < 0.25$, as given by Gaia EDR3.

The first three cuts ensure precise determinations of the G -band, K_s -band, and $W1$ -band absolute magnitudes. The fourth cut is to ensure reliable photometric metallicity estimates. The final cut is to exclude potential stellar binaries, blends, and galaxies. In the second cut, no RRc stars in low-latitude regions are selected, due to the lack of accurate extinction estimates in the disk region. To ensure a sufficient number of RRc stars for the calibration, the definition of the high-latitude region is slightly looser for RRc stars than for type RRab stars. Finally, a total of 825 type RRab and 100 type RRc stars are selected for the calibrations (hereafter, the RRL_CAL_DIS sample).

The distances of the selected RRLs are derived from the parallax measurements in Gaia EDR3 by a Bayesian method, like that used by Huang et al. (2021a). We note that the zeropoints of the Gaia EDR3 parallaxes have been corrected using the procedures provided by Lindegren et al. (2021), which have been independently examined by other studies (e.g., Huang et al. 2021b; Ren et al. 2021; Zinn 2021; Wang et al. 2022a).

3.2.1. M_G –[Fe/H] Relations

We now use the RRL_CAL_DIS sample to calibrate the M_G –[Fe/H] relations for both type RRab and type RRc stars. First, the G -band absolute magnitudes of the sample stars are derived from the parallax-based distances and extinction corrections, assuming $R_G = 2.516$ (Huang et al. 2021c). The uncertainties in M_G are primarily from three sources: the distance errors, the photometric measurement errors of the G band, and an adopted $E(B-V)$ error of 0.05 mag. To ensure the high quality of our calibration samples, we further require that $e_{M_G} \leqslant 0.15$ mag, for both type RRab and type RRc stars. With these cuts, 205 type RRab and 31 type RRc stars remain

in our RRL_CAL_DIS sample stars. A simple linear relation between M_G and [Fe/H] is then adopted:

$$M_G = b [\text{Fe}/\text{H}] + c, \quad (3)$$

where M_G is the reddening corrected G -band absolute magnitude, [Fe/H] is the photometric metallicity estimated from Equations (1) and (2), and b and c are fit coefficients. The resulting fit coefficients for type RRab and type RRc stars are listed in Table 2.

The fitting results for type RRab and type RRc stars are presented in Figures 6 and 7, respectively. In Figure 6, we show that the new calibration from this study (the black line) is consistent with that of Muraveva et al. (2018a). The corresponding absolute G -band magnitudes at [Fe/H] = −1.5 are 0.584 ± 0.036 mag and 0.631 ± 0.103 mag for type RRab and type RRc stars, respectively, which are again in good agreement with the results from Muraveva et al. (2018a). The scatters of the fitting residuals are only 0.12 and 0.10 mag for type RRab and type RRc stars, respectively, which are smaller than the results that have been achieved in most recent calibrations (e.g., Muraveva et al. 2018a; Neeley et al. 2019).

We apply the newly constructed M_G –[Fe/H] relations to estimate the distances for the type RRab and type RRc stars in our final RRL sample. Generally, the extinction corrections are adopted from the SFD98 map. However, for the LMC and SMC regions, a more precise map, provided by Skowron et al. (2021; hereafter, S21), is adopted for these corrections. For the low-latitude region with $|b| \leqslant 25^\circ$, the corrections for $E(B-V)$ are those provided by C22, if available, for type RRab stars. For the member RRLs of GCs (see the details in Section 4.2), the values of $E(B-V)$ are taken from Harris (2010; hereafter, H10).

A summary of the extinction corrections is presented in Table 3. The distances for all our RRL sample stars (115,410 type RRab and 20,463 type RRc stars) are derived in this manner. The uncertainties of the distances are contributed by random and method errors. The random error can be estimated by an MC simulation similar to that mentioned in Section 3.1. For each star, 1000 MC simulations are performed, by

Table 2
 M_G –[Fe/H] and PMZ Relations from the RRL_CAL_DIS Sample

Relation	Mathematical Form	M (mag)	N	σ (mag)
M_G –[Fe/H] ^a	$M_G = (0.350 \pm 0.016)[\text{Fe}/\text{H}] + (1.106 \pm 0.021)$	$0.584 \pm 0.036^{\text{c}}$	205	0.12
M_G –[Fe/H] ^b	$M_G = (0.344 \pm 0.051)[\text{Fe}/\text{H}] + (1.147 \pm 0.074)$	$0.631 \pm 0.103^{\text{c}}$	31	0.10
$PM_{K_s}Z$ ^a	$M_{K_s} = (-2.465 \pm 0.084)\log(P) + (0.161 \pm 0.011)[\text{Fe}/\text{H}]$ – (0.792 ± 0.043)	$-0.341 \pm 0.043^{\text{d}}$	159	0.14
$PM_{W1}Z$ ^a	$M_{W1} = (-2.452 \pm 0.080)\log(P) + (0.179 \pm 0.011)[\text{Fe}/\text{H}]$ – (0.834 ± 0.031)	$-0.413 \pm 0.040^{\text{d}}$	164	0.09

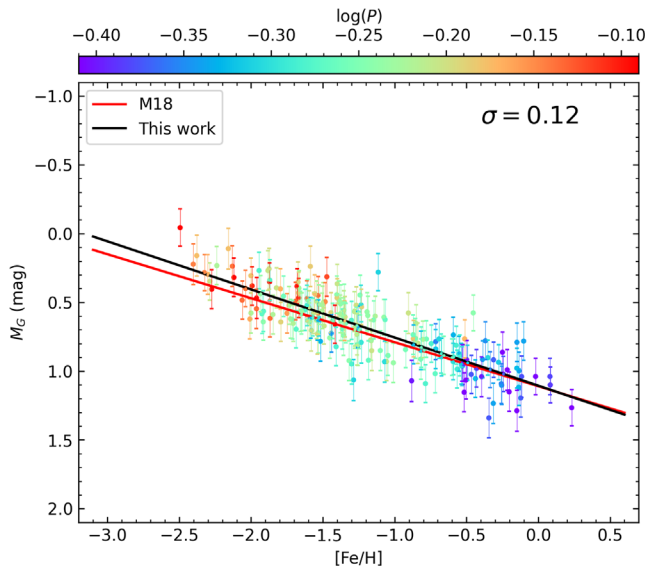
Notes.^a The fitting result is given for type RRab stars.^b The fitting result is given for type RRc stars.^c The absolute magnitudes of type RRab or type RRc stars in different passbands, calculated by adopting a metallicity [Fe/H] = –1.5.^d The absolute magnitudes of type RRab stars in different passbands, calculated by adopting a metallicity [Fe/H] = –1.5 and $P = 0.5238$ days.

Figure 6. M_G –[Fe/H] distribution of 205 type RRab stars from our RRL_CAL_DIS sample, color-coded by the pulsation period on a logarithmic scale, as shown in the color bar. The black line represents the best-fit result. The red line is the fit result from Muraveva et al. (2018a). The standard deviation of the fitting residuals is marked in the top right corner.

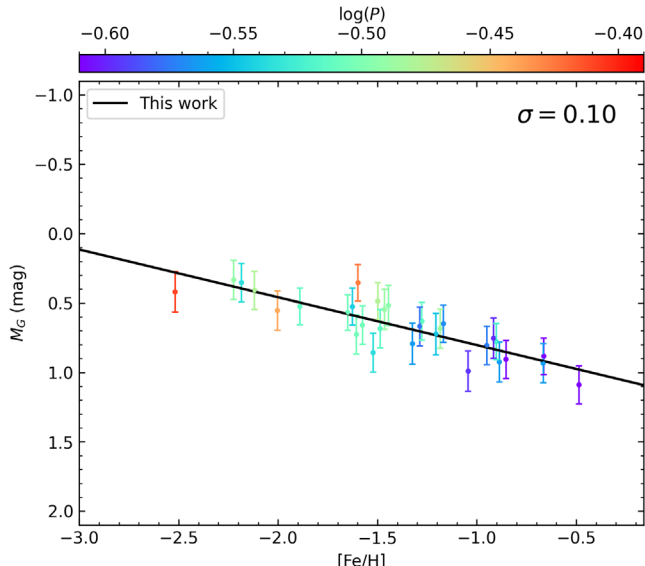


Figure 7. The same as Figure 6, but for type RRc stars.

Table 3
Summary of $E(B - V)$ Determinations

Region	Method	Flag	N
All sky	SFD98	sfd98	31,074 ^a / 19,097 ^b
$ b < 25^\circ$	C22	c22	64,364 ^a / 0 ^b
Magellanic Clouds	S21	s21	19,541 ^a / 1366 ^b
GCs	H10	h10	431 ^a / 78 ^b

Notes.^a The number of type RRab stars.^b The number of type RRc stars.

sampling the uncertainties of the fit coefficients, the G -band magnitudes, and the photometric metallicities, as well as a fixed uncertainty of 0.05 mag for $E(B - V)$. The random error of each star is calculated from the distribution yielded from the MC simulations. The method errors are set to 0.12 and 0.10 mag for type RRab and type RRc stars, respectively, adopted from the dispersions of the calibrated relations mentioned above. The typical distance uncertainties are 9.91% and 9.77% for type RRab and type RRc stars, respectively.

3.2.2. Near-IR PMZ Relations

The PMZ relations for RRLs have been studied by many authors (e.g., Bono et al. 2003; Muraveva et al. 2015, 2018a, 2018b; Sesar et al. 2017a) in the near-IR Two Micron All Sky Survey K_s and Wide-field Infrared Survey Explorer $W1$ passbands. Here, we aim to recalibrate the $PM_{K_s}Z$ and $PM_{W1}Z$ relations for type RRab stars, using our RRL_CAL_DIS sample. The absolute magnitudes at K_s and $W1$ are derived for 823 type RRab stars in both bands, by assuming $R_{K_s} = 0.306$ and $R_{W1} = 0.186$ from Yuan et al. (2013). To ensure the quality of the PMZ relations, we remove stars with absolute magnitude uncertainties that are greater than 0.08 mag in either the K_s or the $W1$ bands, leaving 159 and 164 type RRab stars, respectively. A simple 2D linear function is adopted for the PMZ relations:

$$M_{K_s/W1} = d \log(P) + e [\text{Fe}/\text{H}] + f, \quad (4)$$

where $M_{K_s/W1}$ is the K_s - or $W1$ -band absolute magnitude, $\log(P)$ is the logarithm of the pulsation period, $[\text{Fe}/\text{H}]$ is the photometric metallicity, and d , e , and f are the fit coefficients. The resulting fit coefficients of the $PM_{K_s}Z$ and $PM_{W1}Z$

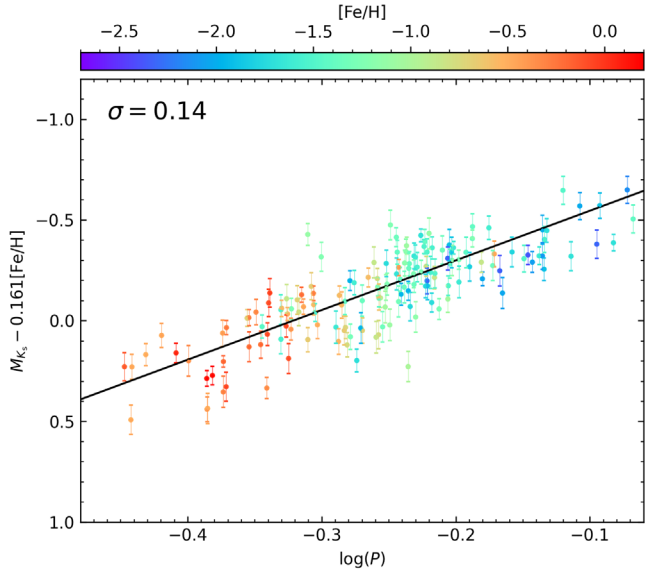


Figure 8. The $PM_{K_s}Z$ relation for 159 type RRab stars, color-coded by metallicity, as shown in the color bar. The black line represents the best-fit result. The standard deviation of the fitting residuals is marked in the top left corner.

relations are listed in Table 2; the fits are shown in Figures 8 and 9, respectively. Our PMZ relations yield residual rms values of 0.14 and 0.09 mag in the K_s and W_1 bands, which again are better than the results of most recent efforts (e.g., Muraveva et al. 2018a; Neeley et al. 2019). For the $PM_{K_s}Z$ relation, the slope of the pulsation period is consistent with those from previous empirical calibration studies (Sollima et al. 2006, 2008; Muraveva et al. 2015, 2018a; Neeley et al. 2019; Muhie et al. 2021) and those given by theoretical studies (Catelan et al. 2004). The relation exhibits a mild metallicity dependence, which is again in agreement with the results of previous empirical calibrations (Muraveva et al. 2018a; Neeley et al. 2019) and theoretical studies (Catelan et al. 2004; Marconi et al. 2015). For the PW_1Z relation, the slope of the period term is consistent with previous results (Dambis et al. 2014; Sesar et al. 2017a; Muraveva et al. 2018a; Neeley et al. 2019; Muhie et al. 2021), and the coefficient of the metallicity term agrees with the results of Muraveva et al. (2018a) and Neeley et al. (2019). The corresponding K_s - and W_1 -band absolute magnitudes at $[Fe/H] = -1.5$ and the pulsation period $P = 0.5238$ days are presented in Table 2. These values are consistent with those given by Muraveva et al. (2018a) and Muhie et al. (2021).

4. Validation of Metallicity and Distance Estimates

In this section, the photometric metallicity estimates in this study are compared to other photometric and spectroscopic estimates from the literature.

4.1. Validation of Photometric Metallicity from Other Spectroscopic Samples

Recently, Dékány & Grebel (2022; hereafter D22) have derived photometric metallicities for nearly 60,000 type RRab stars directly from their light curves as provided by Gaia DR2,

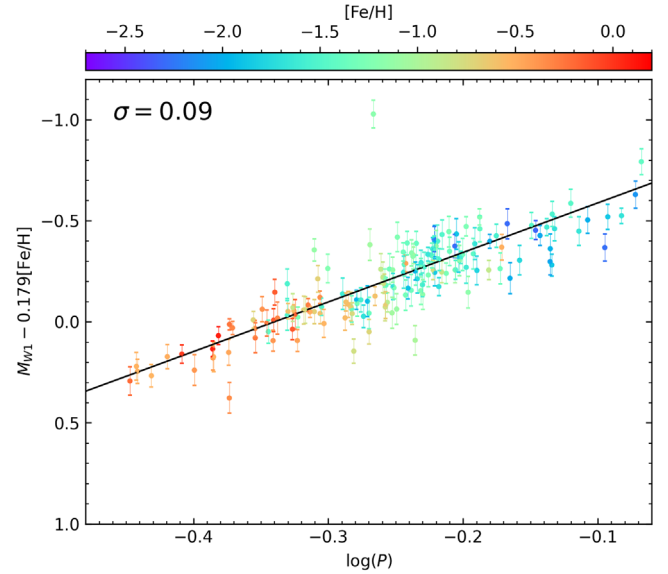


Figure 9. The same as Figure 8, but for the $PM_{W_1}Z$ relation of 164 type RRab stars.

using a deep learning technique. The metallicity of the training sample was adopted from I -band photometric estimates, which were well calibrated by stars with metallicities measured from HRS (Dékány et al. 2021). Here, our photometric metallicities for type RRab stars are compared to those from D22, based on the 49,969 stars in common, with the result being shown in Figure 10(a). The comparison shows a mild offset of 0.17 dex (this work minus D22), plus a scatter of 0.19 dex, implying reasonable consistency between this work and D22. The offset is mainly from the bias of the D22 metallicity scale, if we trust the scale of metallicity measured from HRS (see Figure 11).

By using 84 stars with metallicities determined by Layden (1994; hereafter, L94) from low-to-moderate-resolution spectra, Iorio & Belokurov (2021; hereafter, IB21) recalibrated the linear $P-\phi_{31}-[Fe/H]$ relation for type RRab stars, using the period and ϕ_{31} from Gaia Data Release 2 (Clementini et al. 2019). They also recalibrated the same relation for type RRc stars, using GC members with metallicities taken from H10. We then compare the metallicities in this work to those yielded by the relations of IB21 for 115,410 type RRab stars (the middle panel of Figure 10) and 20,463 type RRc stars (the right panel of Figure 10) from Gaia DR3. In general, our photometric estimates agree very well with those of IB21, with an overall scatter of around 0.16 dex. However, we note that the metallicity scale of IB21 is systematically higher than that in this work, by about 0.1 dex. Moreover, a significant systematic trend along $[Fe/H]$ is detected for both type RRab and type RRc stars. The offset (IB21 minus this work) is about -0.5 dex at $[Fe/H]$ around 0.5 and about 0.5 dex at $[Fe/H]$ around -3.0 for type RRab stars. For type RRc stars, the offset is minor at the metal-rich range, while it is significant up to 0.4 dex at the metal-poor end ($[Fe/H] \sim -3.0$). From checks with the HRS measurements (see Figure 11), the overall offset as well as the systematic trend, as found by our comparisons, are mainly due to the calibrations of IB21.

Dékány et al. (2021; hereafter D21) presented a bibliographical compilation of 183 RRab and 49 RRc stars with

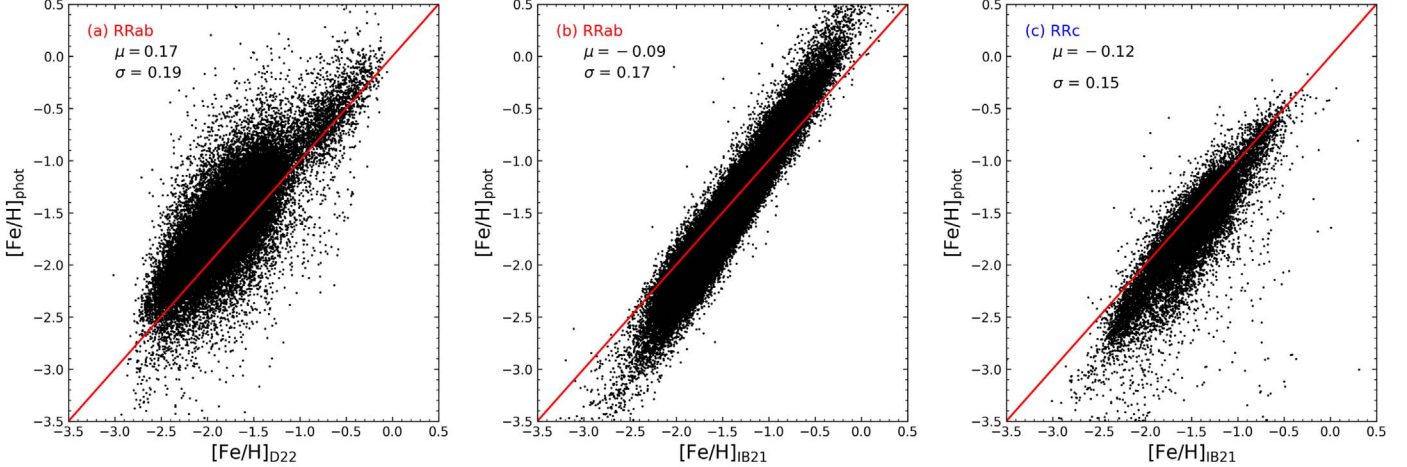


Figure 10. (a) Comparison between the metallicities for type RRab stars from this work and those measured by D22. (b) Similar to (a), but comparing between this work and IB21. (c) Similar to (b), but for type RRc stars. The values of the means and standard deviations of the metallicity differences (this work minus D22 or IB21) are marked in the top left corners of each panel.

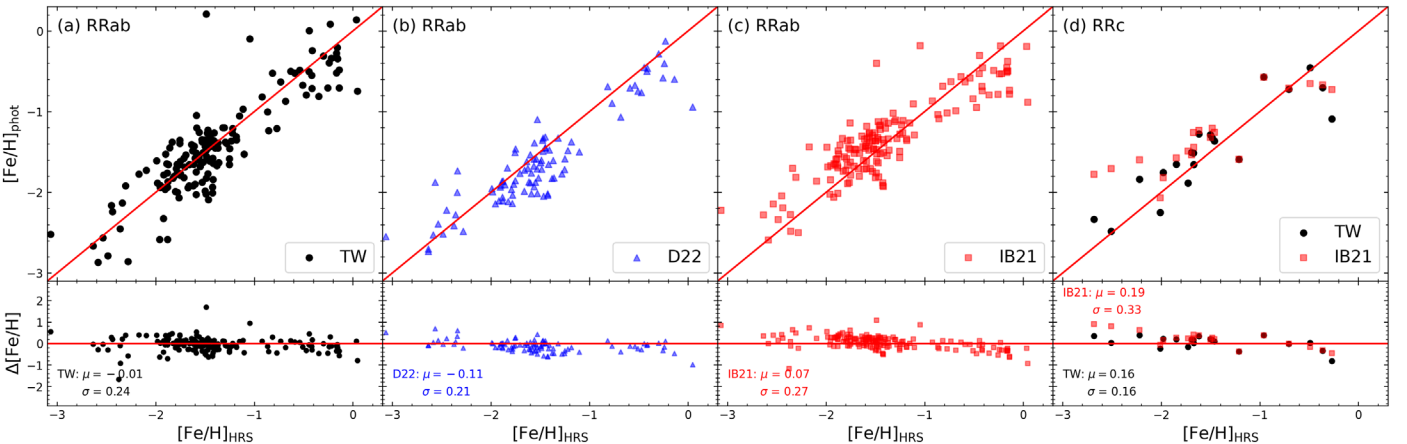


Figure 11. (a) Comparison between the metallicities for type RRab stars from this work (TW) and those measured from HRS (Dékány et al. 2021). (b) Similar to (a), but comparing between D22 and HRS. (c) Similar to (a), but comparing between IB21 and HRS. (d) Similar to (a), but comparing type RRc stars between TW (the black dots), IB21 (the red squares), and HRS. The metallicity differences $\Delta[\text{Fe}/\text{H}]$ (TW/D22/IB21 minus HRS) are shown in the lower part of each panel, with the means and standard deviations marked in the bottom left corners.

metallicity measurements from HRS, covering the range $-3.1 \lesssim [\text{Fe}/\text{H}] \lesssim 0.2$. All the metallicities are carefully calibrated to the reference scale established by Crestani et al. (2021). These stars are therefore used to examine the performances of our photometric estimates of metallicity, as well as those of D22 and IB21. The comparisons are presented in Figure 11. For type RRab stars, the metallicities from this work are in excellent agreement with those from HRS, with a negligible offset of -0.01 dex and a dispersion of 0.24 dex. The metallicities of type RRc stars from this work again agree very well with those from HRS, with a scatter of only 0.16 dex, although there exists a mild offset of 0.16 dex (this work minus HRS). The D22 results for type RRab stars are also consistent with those from HRS, with a small dispersion of 0.21 dex, while the scale of D22 is slightly lower than that of HRS, by 0.11 dex. The metallicity comparisons between IB21 and HRS exhibit large scatters of $0.27/0.33$ dex and offsets of $0.09/0.19$ dex (IB21 minus HRS) for type RRab/RRc stars. Moreover, the metallicity differences show a significant trend with $[\text{Fe}/\text{H}]$ (see the right two panels of Figure 11).

4.2. Validation with GCs

The member stars of GCs are expected to be born at the same times and with almost the same metallicities. The RRLs of GCs are therefore selected in this study to test the accuracy of our photometric metallicities and our distance estimates from our newly derived $M_G - [\text{Fe}/\text{H}]$ relations. Prior to these comparisons, we apply the following cuts, to select the member stars of the GCs from our RRL sample:

1. The positions must within 15 half-light radii r_h (from H10) from the center of the GC; and
2. The proper motions must satisfy $|\mu_\alpha - \mu_{\alpha,\text{GC}}| \leq 8 \sigma_{\mu_{\alpha,\text{GC}}}$ and $|\mu_\delta - \mu_{\delta,\text{GC}}| \leq 8 \sigma_{\mu_{\delta,\text{GC}}}$.

The above cuts are applied to 157 GCs in H10. The proper motions and uncertainties for each GC are taken from Vasiliev & Baumgardt (2021).

Finally, to ensure that our estimates of the mean metallicity and the distance of the GCs are reasonably well determined from our RRL sample stars, a minimum number of five type RRab and three type RRc stars are required for selecting the

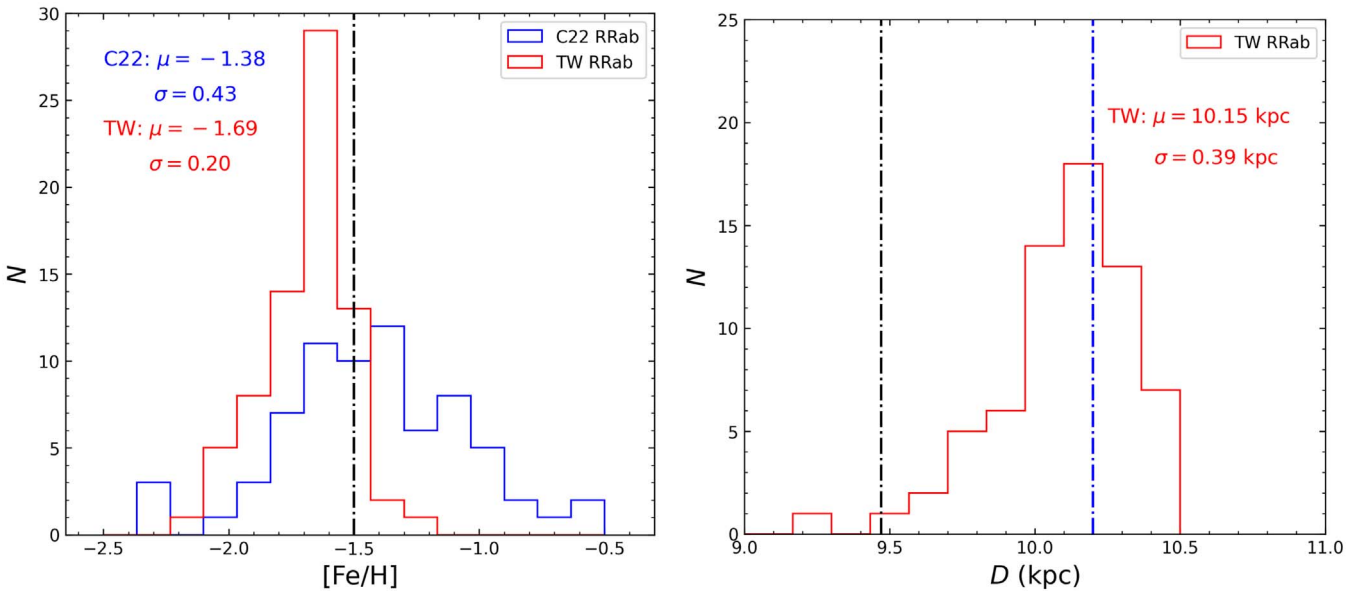


Figure 12. Left: metallicity distributions for the member type RRab stars of NGC 5272, with red for this work (TW) and blue for C22. The metallicity of NGC 5272 from H10 is marked by the dashed-dotted line. The dispersion of the metallicity in this work is much narrower than that in C22. The means and standard deviations of the distributions are marked in the top left corner. Right: similar to the left panel, but for the distance distribution. The distance values for NGC 5272 from B19 and H10 are marked with the black and blue dashed-dotted lines, respectively.

members of each GC. In this way, 431 type RRab and 78 type RRc stars are selected from 26 and 14 GCs, respectively.

The mean metallicity (both for this study and C22) and the distance, as well as their uncertainties (given by the standard deviations of the distributions), are estimated from the distributions of the selected member RRLs for each GC (e.g., see Figure 12). The results are listed in Table 4. As shown in Figure 13, the typical metallicity uncertainties in this study are 0.21 dex and 0.11 dex for type RRab and type RRc stars, respectively, which are significantly smaller than the values of 0.38 dex and 0.13 dex found for C22.

The relative distance errors are mostly within 8% and 5% for the type RRab and type RRc stars, with medians of 4.9% and 2.4%, respectively. The small uncertainties revealed by the GCs, which are even smaller than the typical ones for the full sample, are mainly due to the extinction corrections being nearly nil.

Figure 14 shows a comparison between the metallicities of the GCs from our photometric methods and those from H10. Our results are in excellent agreement with those of H10, with a negligible offset of -0.09 dex and a small scatter of 0.15 dex for type RRab stars, and a mild offset of -0.12 dex and a small scatter of 0.16 dex for type RRc stars. In contrast, the difference between the photometric metallicities for type RRab stars from C22 and those from H10 displays a significant offset of 0.31 dex and a relatively large scatter of 0.18 dex. The photometric metallicities from C22 for type RRc stars are slightly higher than those for the GCs, by 0.09 dex, with a moderate scatter of 0.16 dex. In summary, the accuracies of the photometric metallicities obtained in this study are much higher than those achieved by C22 (especially for type RRab stars).

For the distances, we compare our results to those of Baumgardt et al. (2019; hereafter, B19), which determine accurate kinematic distances for 53 GCs by fitting proper-motion and line-of-sight velocity dispersion profiles to N -body simulations of the individual GCs. The comparison is shown in Figure 14. From an inspection, our derived distances for the

GCs are in excellent agreement with the kinematic distances of B19, with negligible median offsets of the relative distance difference $\Delta D/D$ of $2.6\%/1.8\%$, and small scatters of $5.3\%/4.2\%$, for type RRab/RRc stars, respectively. In addition, our distances are also consistent with the previous work of H10, exhibiting negligible offsets of the relative distance difference $\Delta D/D$ of $-2.8\%/-2.0\%$, and small scatters of $4.3\%/4.3\%$, for type RRab/RRc stars, respectively. We also note that for NGC 1851, IC 4499, NGC 6121, NGC 6171, and NGC 6362, the distances derived from the type RRc stars are in excellent agreement with the results from the type RRab stars, with the relative distance differences being smaller than a few percent.

5. RRL Sample

In this section, we describe the properties and potential applications of our final sample of RRL stars.

Our final RRL sample contains 135,873 RRLs (115,410 type RRab and 20,463 type RRc stars), with precise metallicity and distance estimates from the newly constructed $P-\phi_{31}-R_{21}-[\text{Fe}/\text{H}]$, $P-R_{21}-[\text{Fe}/\text{H}]$, and $M_G-[\text{Fe}/\text{H}]$ relations. The distance distribution of the final RRL sample is shown in Figure 15, with five prominent peaks at heliocentric distances of 8, 26, 50, 64, and 82 kpc, corresponding to the positions of the Galactic bulge, the Sagittarius dwarf galaxy, the LMC, the SMC, and the Sculptor dwarf galaxy, respectively. The sample stars can reach as far as 100 kpc, but most of them are within 30 kpc, except those belonging to the LMC/SMC. We then calculate the 3D positions of our sample stars from their sky positions (l, b) and distances. We use a right-handed Cartesian Galactocentric coordinate system (X, Y, Z), with X pointing toward the Galactic center, Y pointing in the direction of Galactic rotation, and Z pointing toward the north Galactic pole. The position of the Sun is set to $(X, Y, Z) = (-8.34, 0.00, 0.00)$ kpc (Reid et al. 2014).

The spatial distributions of our sample stars in the $X-Z$ and $Y-Z$ planes are presented in Figure 16. The sample covers a large halo volume of $|X| \leq 30$ kpc, $|Y| \leq 30$ kpc, and $|Z| \leq 30$ kpc,

Table 4
Comparison of the Photometric Metallicities and Distances for GCs with Values from H10 and B19

Name	[Fe/H] _{H10}	d_{H10} (kpc)	d_{B19} (kpc)	$\langle [\text{Fe}/\text{H}]_{\text{C22}} \rangle$ (dex)	$\sigma_{[\text{Fe}/\text{H}]_{\text{C22}}}$ (dex)	$\langle [\text{Fe}/\text{H}]_{\text{phot}} \rangle$ (dex)	$\sigma_{[\text{Fe}/\text{H}]_{\text{phot}}}$ (dex)	$\langle d_{\text{phot}} \rangle$ (kpc)	$\sigma_{d_{\text{phot}}}$ (kpc)	N
(a) RRab										
NGC 1851	-1.18	12.1	11.32 ± 0.20	-1.23	0.54	-1.60	0.43	12.04	0.91	5
NGC 3201	-1.59	4.9	4.47 ± 0.18	-1.23	0.38	-1.58	0.19	4.78	0.24	41
Rup 106	-1.68	21.2	...	-1.26	0.24	-1.77	0.11	21.20	0.42	8
NGC 4590	-2.23	10.3	...	-1.87	0.66	-2.10	0.29	10.16	0.59	8
NGC 4833	-1.85	6.6	6.10 ± 0.43	-1.55	0.34	-1.96	0.13	6.21	0.34	5
NGC 5024	-2.10	17.9	...	-1.56	0.62	-2.00	0.18	17.88	0.58	17
NGC 5053	-2.27	17.4	...	-1.68	0.28	-2.07	0.13	16.70	0.16	5
NGC 5272	-1.50	10.2	9.47 ± 0.45	-1.38	0.43	-1.69	0.20	10.15	0.39	74
NGC 5466	-1.98	16.0	...	-1.70	0.31	-2.01	0.21	15.71	0.33	11
IC 4499	-1.53	18.8	...	-1.40	0.48	-1.73	0.28	19.35	1.00	46
NGC 5824	-1.91	32.1	...	-1.26	0.77	-1.84	0.25	30.83	1.48	5
NGC 5904	-1.29	7.5	7.58 ± 0.14	-1.28	0.48	-1.60	0.27	7.35	0.37	14
NGC 6121	-1.16	2.2	1.96 ± 0.04	-1.00	0.16	-1.39	0.12	2.05	0.17	5
NGC 6171	-1.02	6.4	5.92 ± 0.38	-0.58	0.36	-1.14	0.12	5.88	0.37	7
NGC 6229	-1.47	30.5	...	-1.04	0.31	-1.47	0.17	29.38	0.94	11
NGC 6266	-1.18	6.8	6.40 ± 0.18	-0.72	0.37	-1.30	0.26	6.15	0.67	11
NGC 6362	-0.99	7.6	7.34 ± 0.31	-0.79	0.34	-1.29	0.25	7.26	0.26	13
NGC 6401	-1.02	10.6	...	-0.63	0.28	-1.11	0.18	8.80	0.63	7
NGC 6402	-1.28	9.3	9.31 ± 0.50	-0.73	0.33	-1.27	0.22	8.60	0.44	14
NGC 6426	-2.15	20.6	...	-1.72	0.43	-2.15	0.10	20.73	0.45	8
NGC 6584	-1.50	13.5	...	-1.08	0.38	-1.54	0.26	13.16	0.55	24
NGC 6715	-1.49	26.5	24.15 ± 0.38	-1.26	0.75	-1.57	0.42	26.94	1.76	15
NGC 6934	-1.47	15.6	14.57 ± 1.43	-1.33	0.42	-1.67	0.22	15.60	0.54	29
NGC 6981	-1.42	17.0	...	-1.38	0.31	-1.70	0.13	16.84	0.45	24
NGC 7006	-1.52	41.2	...	-1.35	0.51	-1.65	0.24	42.11	1.69	11
NGC 7078	-2.37	10.4	10.21 ± 0.13	-2.01	0.45	-2.21	0.17	10.69	0.65	13
(b) RRc										
NGC 1851	-1.18	12.1	11.32 ± 0.20	-1.10	0.10	-1.53	0.04	11.97	0.27	3
NGC 4590	-2.23	10.3	...	-2.20	0.06	-2.35	0.15	10.60	0.23	8
NGC 5053	-2.27	17.4	...	-1.96	0.33	-2.21	0.15	17.33	0.72	4
NGC 5272	-1.50	10.2	9.47 ± 0.45	-1.52	0.13	-1.56	0.24	9.71	0.41	9
NGC 5466	-1.98	16.0	...	-1.77	0.30	-1.72	0.23	15.27	0.50	3
IC 4499	-1.53	18.8	...	-1.79	0.17	-1.84	0.09	19.28	0.22	6
NGC 6121	-1.16	2.2	1.96 ± 0.04	-0.98	0.13	-1.29	0.10	2.07	0.10	3
NGC 6171	-1.02	6.4	5.92 ± 0.38	-0.97	0.08	-1.19	0.10	5.76	0.15	6
NGC 6266	-1.18	6.8	6.40 ± 0.18	-1.12	0.06	-1.28	0.09	6.48	0.59	3
NGC 6362	-0.99	7.6	7.34 ± 0.31	-0.95	0.13	-1.22	0.16	7.19	0.19	8
NGC 6402	-1.28	9.3	...	-0.87	0.29	-1.29	0.18	8.93	0.19	5
NGC 6584	-1.50	13.5	...	-1.50	0.15	-1.62	0.11	13.31	0.19	4
NGC 6638	-0.95	9.4	...	-1.00	0.11	-1.28	0.04	9.65	0.18	3
NGC 7078	-2.37	10.4	10.21 ± 0.13	-2.16	0.28	-2.47	0.09	11.06	0.19	13

Note. Column (1): cluster identification number. Columns (2) and (3): the metallicities and distances of the GCs from H10. Column (4): the distances and errors of the GCs from B19. Columns (5) to (10): the mean values and their errors from C22 and our photometric metallicities and distances for the GCs (see Section 4.2). Column (11): the number of GC member RRL stars that passed the cuts discussed in Section 4.2.

with a sufficient number of stars to explore questions relating to the Galactic structure and the nature of the stellar populations in this region. Table 5 lists the columns that are included in the final online sample catalog, which is also available on Zenodo: 10.5281/zenodo.7471144.

This sample will clearly be very useful for studying the structure and the chemical and kinematic properties of the Galactic halo. For example, the sample has already been applied to find substructures and to study their chemical properties (Wang et al. 2023). To show the potential power of this sample, we use it to derive the distance moduli and to consider the chemical properties of the LMC and SMC, as an example.

The LMC and SMC are the two largest satellite galaxies of the Milky Way, located at distances of about 50 and 60 kpc from the Sun, respectively. They are regarded as cornerstones of the cosmological distance ladder, and it is therefore of vital importance that we obtain very accurate and consistent distances for the two systems, by means of different tracers using different methods. Here, we derive distances for the LMC and SMC from the type RRab stars in our final sample. Member stars of the LMC and SMC are selected by requiring our type RRab stars to lie within radii of 20° and 10° from the centers of the two systems, respectively. The positions of the centers of the LMC and SMC are $(\alpha_{\text{C,LMC}}, \delta_{\text{C,LMC}}) = (81^\circ 28', -69^\circ 78')$, as defined by van der Marel (2001), and $(\alpha_{\text{C,SMC}},$

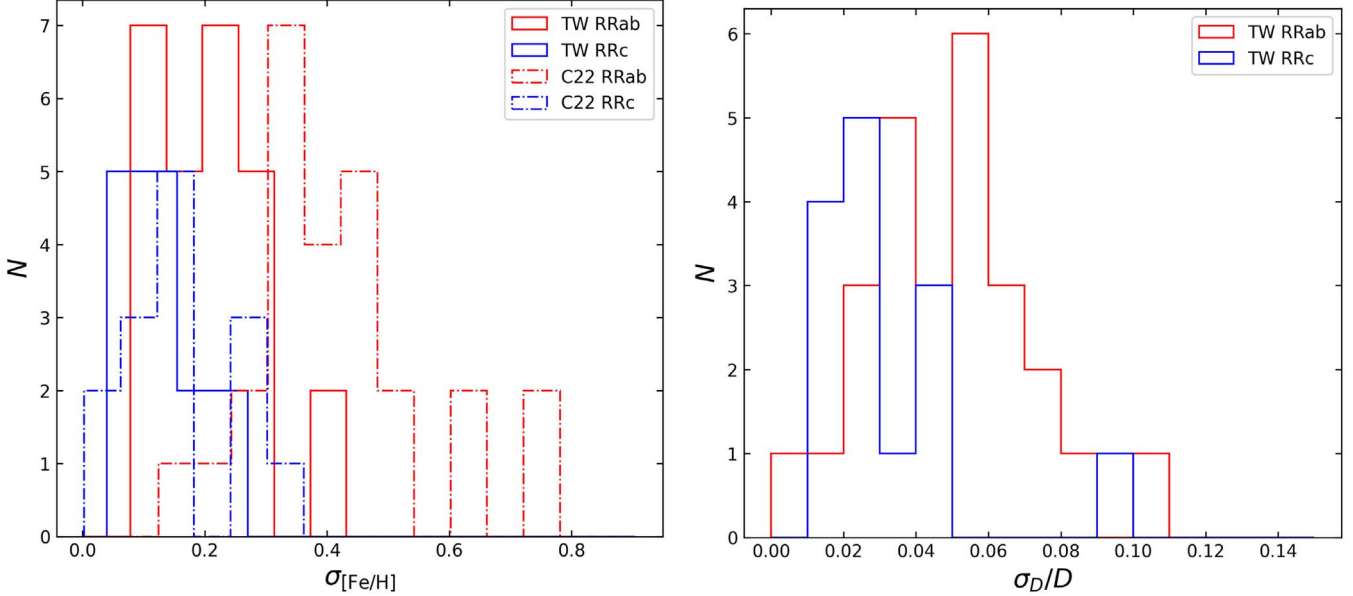


Figure 13. Left: distributions of the metallicity uncertainties estimated from the members of GCs, with red for the type RRab stars and blue for the type RRc stars, with the solid lines for this work (TW) and the dashed-dotted lines for C22. Right: similar to the left panel, but for the relative distance uncertainties.

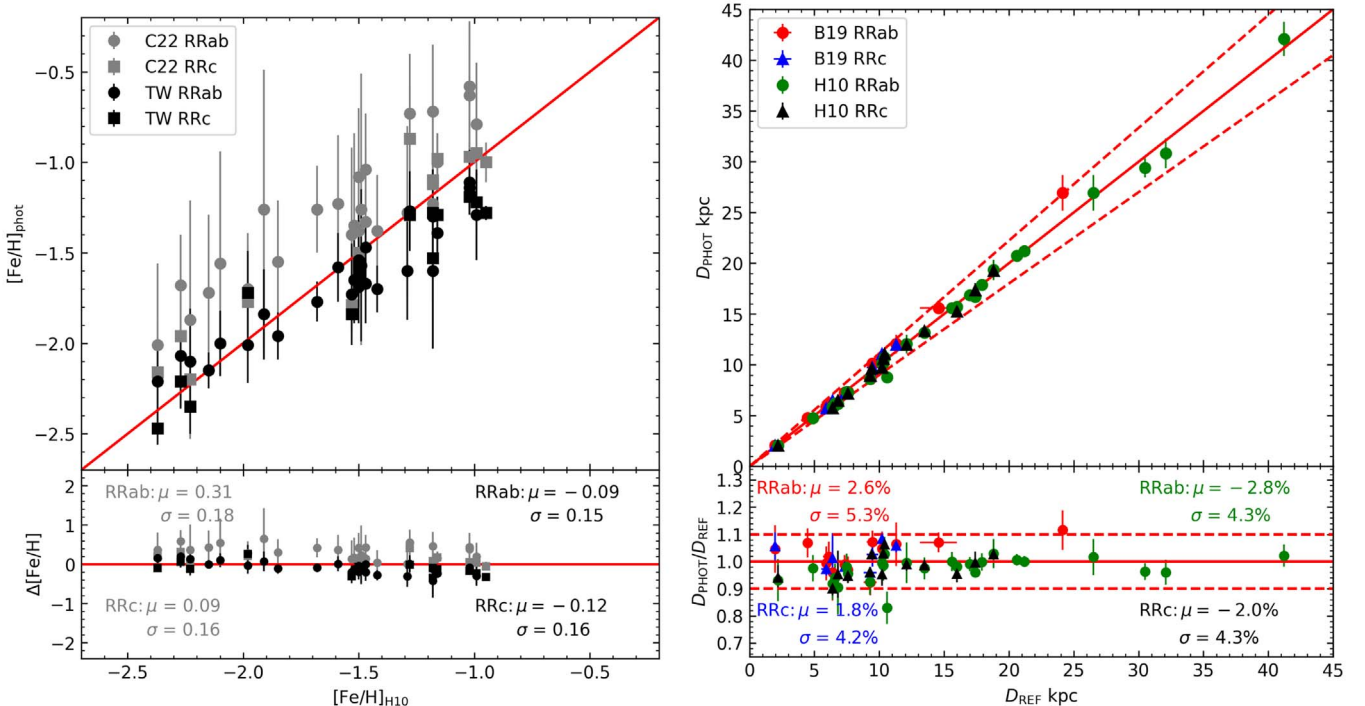


Figure 14. Left: comparison between our estimated photometric metallicities for the GCs and those from H10. The black dots and squares indicate the photometric metallicities of the GCs derived from type RRab and type RRc stars, respectively, by our photometric method. The photometric metallicities of the GCs (the gray dots and squares) from C22 are also shown for comparison. The metallicity differences $\Delta[\text{Fe}/\text{H}]$ (in the sense of this work or C22 minus H10) are shown in the lower part of the panel, with the means and standard deviations of the differences marked. Right: comparison of the estimated distances for the GCs with those from B19 and H10. The dots and triangles indicate the distances for the GCs derived from type RRab and type RRc stars, respectively, by our $M_G - [\text{Fe}/\text{H}]$ relation. The dashed red lines mark $D_{\text{PHOT}} = 1.1D_{\text{REF}}$ and $D_{\text{PHOT}} = 0.9D_{\text{REF}}$, respectively. The ratios $D_{\text{PHOT}}/D_{\text{REF}}$ are shown in the lower part of the panel, with the means and standard deviations of the relative difference $\Delta D/D$ marked in the four corners.

$\delta_{\text{C,SMC}} = (12^{\circ}80, -73^{\circ}15)$, as defined by Cioni et al. (2000), respectively. In this way, 15,038 and 2696 type RRab stars with distance errors smaller than 12% are selected in the LMC and SMC, respectively. Distance moduli of $\mu_0 = 18.503 \pm 0.001$ (stat) ± 0.040 (syst) mag and $\mu_0 = 19.030 \pm 0.003$ (stat) ± 0.043 (syst) are derived for the LMC and SMC, respectively, from the selected type RRab stars (see Figure 17).

A summary of our error budget is available in Table 6. The standard deviations of the distance distributions are 0.153 and 0.170 mag, respectively, for the LMC and SMC, which are mainly contributed by the physical extensions of the two systems themselves. The results are in excellent agreement with previous measurements from tracers such as Cepheids (e.g., Freedman et al. 2012; Scowcroft et al. 2016), RRLs (Neeley

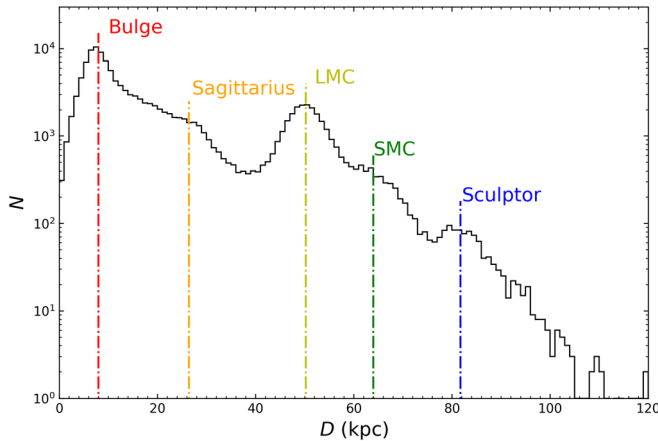


Figure 15. Histogram of the distances for 115,410 type RRab and 20,463 type RRc stars. The red, orange, yellow, green, and blue dashed lines mark the positions of the Galactic bulge, the Sagittarius dwarf galaxy, the LMC, the SMC, and the Sculptor dwarf galaxy, respectively.

Table 5
Description of the Final Sample

Field	Description	Unit
Gaia	Unique source identifier for Gaia DR3 [source_id]	...
RAdeg	Right ascension from Gaia DR3 (ICRS at Epoch = 2016)	degrees
DEdeg	Decl. from Gaia DR3 (ICRS at Epoch = 2016)	degrees
[Fe/H]	Photometric metallicity	...
e_[Fe/H]	Uncertainty of the photometric metallicity	dex
MGmag	G-band absolute magnitude	mag
e_MGmag	Uncertainty of the G-band absolute magnitude	mag
EBV	Value of $E(B - V)$	mag
e_EBV	Flag to indicate the source of $E(B - V)$, which takes the values "sfd98," "c22," "s21," and "h10"	...
Dist-Phot	Distance	kpc
e_Dist-Phot	Uncertainty of the distance	kpc
Type	Type of RRL star, which takes the values "RRab" and "RRc"	...

Note. The final RRL sample with the items defined above is provided in the online Journal, while a copy has also been deposited on Zenodo: [10.5281/zenodo.7471144](https://zenodo.3528114/).

(This table is available in its entirety in machine-readable form.)

et al. 2019), eclipsing binaries (Pietrzyński et al. 2019; Graczyk et al. 2020), and the reported mean values of different tracers (de Grijs et al. 2014; de Grijs & Bono 2015).

We also consider the question of whether metallicity gradients exist in the LMC or SMC. We employ the following transformation equations (van der Marel & Cioni 2001; Weinberg & Nikolaev 2001) to calculate the 3D coordinates for each type RRab star in the LMC or SMC:

$$\begin{aligned} x &= -d \times \cos(\delta)\sin(\alpha - \alpha_C), \\ y &= d \times [\sin(\delta)\cos(\delta_C) \\ &\quad - \cos(\delta)\sin(\delta_C)\cos(\alpha - \alpha_C)], \\ z &= d \times [\cos(\delta)\cos(\delta_C)\cos(\alpha - \alpha_C) \\ &\quad + \sin(\delta)\sin(\delta_C)] - D_C, \end{aligned} \quad (5)$$

where d is the heliocentric distance of each type RRab star, α_C and δ_C are the equatorial coordinates of the LMC/SMC

Table 6
Summary of the Error Budgets for the Distance and Metallicity Estimates of the LMC and SMC

Description	Term	LMC	SMC
Distance			
Statistical Uncertainties (per star)			
Mean G -band magnitude uncertainty	σ_G	0.014	0.013
Extinction ^a	σ_{AG}	0.103	0.069
G -band absolute magnitude	σ_{MG}	0.134	0.137
Total statistical uncertainty	...	0.001	0.003
Systematic Uncertainties			
Gaia photometric calibration ^b	σ_{ZPG}	0.004	0.004
Extinction ^a	$\sigma_{AG,\text{sys}}$	0.020	0.020
M_G –[Fe/H] relation metallicity constant ^c	$x\sigma_b$	0.027	0.032
M_G –[Fe/H] relation zeropoint	σ_c	0.021	0.021
Total systematic uncertainty	...	0.040	0.043
Metallicity			
Statistical Uncertainties (per star)			
Metallicity	$\sigma_{[\text{Fe}/\text{H}]}$	0.361	0.371
Total statistical uncertainty	...	0.003	0.008
Systematic Uncertainties			
P – ϕ_{31} – R_{21} –[Fe/H] relation fit coefficients ^d	σ_{a_0}	0.002	0.002
	$y\sigma_{a_1}$	0.015	0.016
	$z\sigma_{a_2}$	0.010	0.010
	$t\sigma_{a_3}$	0.014	0.013
Total systematic uncertainty	...	0.023	0.023

Notes.

^a The typical uncertainties of the extinction and extinction scale are taken from S21.

^b The typical calibration uncertainty of the Gaia G band is taken from Yang et al. (2021).

^c Here, x represents the mean metallicity of the LMC/SMC, as given in Section 5.

^d Here y , z , and t represent the mean period, ϕ_{31} , and R_{21} of type ab RRLs in the LMC/SMC, taking values of 0.581/0.598 days, 2.087/2.095, and 0.461/0.432, respectively.

centers, and D_C is the mean distance of the LMC/SMC, as given by our determinations above, i.e., $D_{C,\text{LMC}} = 50.19$ kpc for the LMC and $D_{C,\text{SMC}} = 63.97$ kpc for the SMC. The radial distances from the LMC/SMC centers, $r = \sqrt{x^2 + y^2 + z^2}$, are then derived for the type RRab stars in the LMC/SMC. To obtain a reliable metallicity trend with the radial distance r , we apply the following cuts to the selected type RRab stars: (i) the photometric metallicity lies in the range of $-3.5 \leq [\text{Fe}/\text{H}] \leq 0.5$ and has uncertainties smaller than 0.5 dex; (ii) the distance errors are smaller than 12%; and (iii) $r \leq 14.5$ kpc. After applying these cuts, 14,242 and 2446 type RRab stars are left in the LMC and SMC, respectively.

The metallicity distributions, as a function of r , for the LMC/SMC are shown in Figure 18. For the LMC, the mean value of the metallicity is $[\text{Fe}/\text{H}] = -1.709 \pm 0.003$ (stat) ± 0.023 (syst), in agreement with the estimate of $[\text{Fe}/\text{H}] = -1.59 \pm 0.31$ by Skowron et al. (2016; hereafter S16). Generally, the metallicity distribution shows a negative slope for $r \leq 5$ kpc, then it tends to be flat for $5 < r < 7$ kpc, and then it again presents a negative gradient for $r > 7$ kpc. Within the inner 5 kpc, we find a metallicity gradient of -0.029 ± 0.004 dex kpc⁻¹, which is steeper than those found

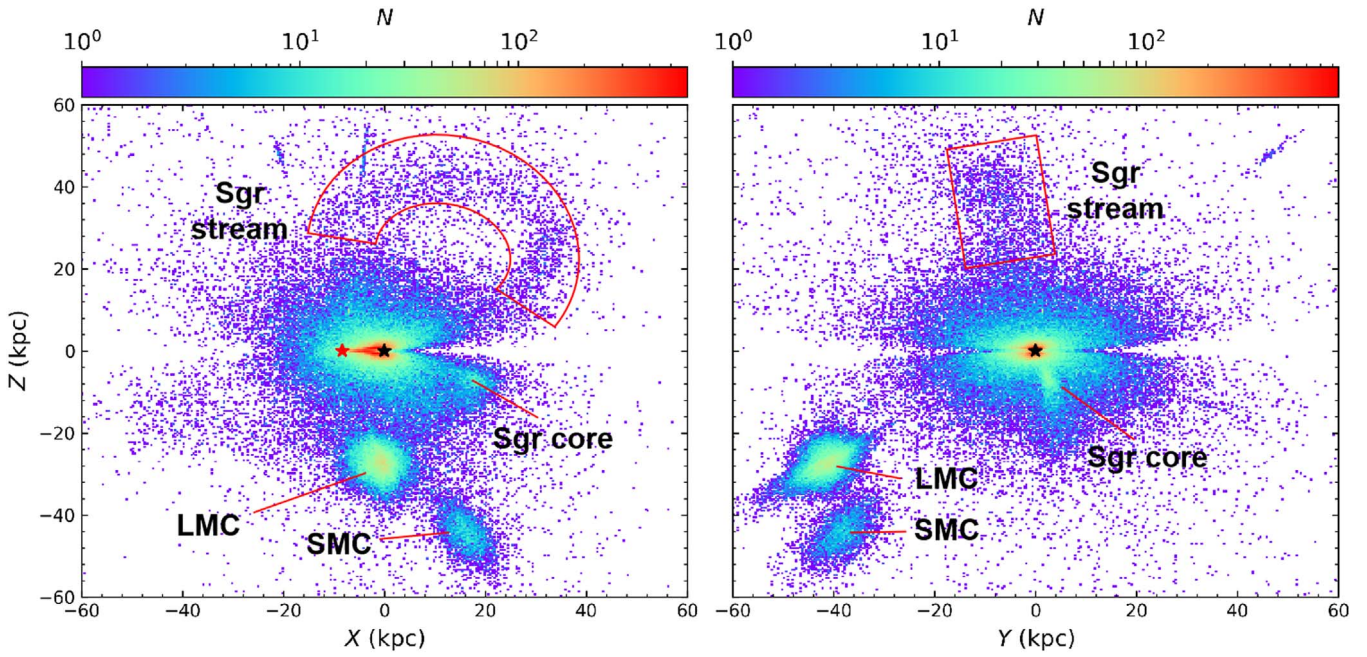


Figure 16. Spatial distributions of our final RRL sample stars in the X - Z (left) and Y - Z (right) planes. The Galactic center and the Sun are represented by the black and red stars, respectively. The stellar number densities (in bin sizes of 0.4 kpc for both axes) are represented by the top color bars. The well-known satellites and structures—e.g., LMC, SMC, and the Sagittarius core and stream—are clearly seen.

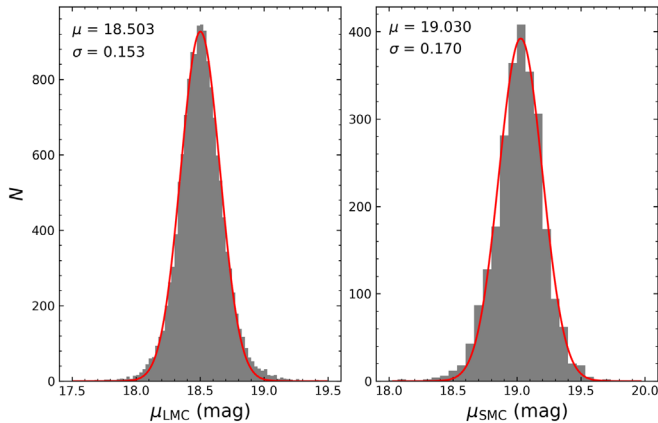


Figure 17. Left: histogram of the distance moduli for all type RRab stars selected in the LMC. The red line shows the Gaussian fit to the distribution, with the mean and the dispersion of the Gaussian marked in the top left corner. Right: the same as the left panel, but for the SMC.

in previous studies using RRL stars (Feast et al. 2010; Wagner-Kaiser & Sarajedini 2013), but consistent with S16’s result within 1σ . The metallicity gradient is nearly flat around $r_{\text{LMC}} = 6$ kpc. The slope of the gradient is -0.012 ± 0.005 dex kpc $^{-1}$ for r beyond 7 kpc. Excluding the final bin, with large uncertainties, the slope of the gradient becomes -0.018 ± 0.007 dex kpc $^{-1}$, which is smaller than the result of -0.047 ± 0.003 dex kpc $^{-1}$ from Cioni (2009), using asymptotic giant branch (AGB) stars in the same region. The overall slope is -0.024 ± 0.001 dex kpc $^{-1}$ for the entire LMC, which is consistent with S16’s value of -0.019 ± 0.002 dex kpc $^{-1}$. For the SMC, the mean value of the metallicity is $[\text{Fe}/\text{H}] = -1.999 \pm 0.008$ (stat) ± 0.023 (syst), which is also in agreement with S16’s result ($[\text{Fe}/\text{H}] = -1.85 \pm 0.33$). We find that the SMC exhibits a very weak metallicity gradient of -0.007 ± 0.003 dex kpc $^{-1}$. This trend is similar to previous

results that have been derived from AGB stars, stellar clusters, and type RRab stars (Cioni 2009; Parisi et al. 2009; Deb et al. 2015; S16).

6. Summary

In this paper, using a training sample of 2687 RRLs (2046 type RRab and 641 type RRc stars), with accurate pulsation periods, P , Fourier parameters, ϕ_{31} , R_{21} , and metallicity measurements, $[\text{Fe}/\text{H}]$, from Gaia, LAMOST, and the Sloan Digital Sky Survey, new $P-\phi_{31}-R_{21}-[\text{Fe}/\text{H}]$ and $P-R_{21}-[\text{Fe}/\text{H}]$ relations are derived for type RRab and type RRc stars, respectively. Precise photometric metallicities for the 135,873 RRLs (115,410 type RRab and 20,463 type RRc stars) are derived from the constructed relations. Comprehensive external checks demonstrate no significant offsets between our photometric metallicities; the typical precisions are 0.24 and 0.16 dex for type RRab and type RRc stars, respectively. From about hundreds of local bright RRLs with photometric metallicity estimates and accurate distance estimates from Gaia parallaxes, the G -band absolute magnitude–metallicity relations and near-IR PMZ relations are recalibrated. With the newly constructed $M_G-[\text{Fe}/\text{H}]$ relations, the distances for all 135,873 RRLs with photometric metallicity estimates are derived, with a typical uncertainty of 9%–10% (depending on the errors of the extinction corrections).

To demonstrate the power of this sample, we present distance measurements and chemical studies of the LMC and SMC, as an example. Using more than 10,000 type RRab stars, distance moduli of $\mu_0 = 18.503 \pm 0.001$ (stat) ± 0.040 (syst) mag and $\mu_0 = 19.030 \pm 0.003$ (stat) ± 0.043 (syst) mag are found for the LMC and SMC, respectively, which are consistent with previous measurements. In addition, mean metallicities of $[\text{Fe}/\text{H}] = -1.709 \pm 0.003$ (stat) ± 0.023 (syst) for the LMC and $[\text{Fe}/\text{H}] = -1.999 \pm 0.008$ (stat) ± 0.023 (syst) for the SMC are found, which are again in agreement with the results from previous studies. Moreover, we identify a

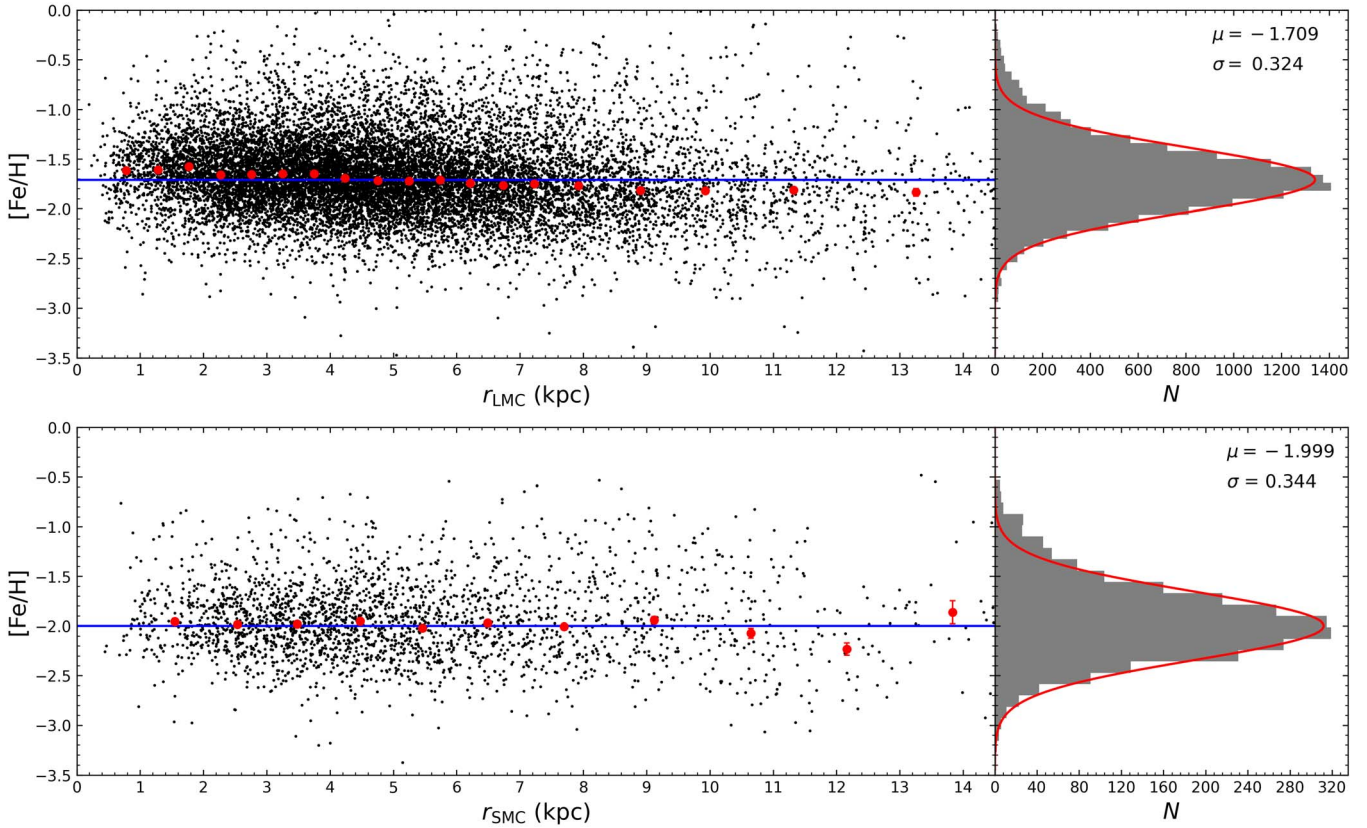


Figure 18. Top: the distribution of the metallicity, as a function of the radial distance from the LMC center (left), with a histogram of the metallicity for 14,242 type RRab stars in the LMC (right). The values of the mean metallicity and the standard deviation derived from a Gaussian fit (the red line) are shown in the top right of the right panel. The mean metallicity is illustrated by the blue line in the left panel. The large red circles mark the median metallicity values for each radial bin, with bin sizes in r_{LMC} of 0.5 kpc for $1 \leq r_{\text{LMC}} \leq 7.5$ kpc, 1 kpc for $r_{\text{LMC}} < 1$ kpc and $7.5 < r_{\text{LMC}} < 10.5$ kpc, and 2 kpc for $r_{\text{LMC}} \geq 10.5$ kpc. Bottom: the same as the top, but for 2446 type RRab stars, with bin sizes in r_{SMC} of 1 kpc for $2 \leq r_{\text{SMC}} \leq 7$ kpc, 1.5 kpc for $r_{\text{SMC}} > 7$ kpc, and 2 kpc for $r_{\text{SMC}} < 2$ kpc.

mild gradient of $-0.024 \pm 0.001 \text{ dex kpc}^{-1}$ for the entire LMC, while the SMC exhibits a nearly flat metallicity gradient of $-0.007 \pm 0.003 \text{ dex kpc}^{-1}$.

We thank an anonymous referee for the helpful comments. This work is supported by the National Natural Science Foundation of China, grant Nos. 11903027, 11973001, 11833006, U1731108, 12090040, and 12090044, and the National Key R & D Program of China, grant No. 2019YFA0405500. Y.H. and X.Y.L. are supported by Yunnan University, grant Nos. C17622010006 and 2021Z015, respectively. T.C.B. acknowledges partial support for this work via grant No. PHY 14-30152, from the Physics Frontier Center/JINA Center for the Evolution of the Elements (JINA-CEE), awarded by the US National Science Foundation. H.W.Z. acknowledges science research grants from the China Manned Space Project, No. CMS-CSST-2021-B03.

This work has made use of data from the European Space Agency (ESA) mission Gaia (<https://www.cosmos.esa.int/gaia>), processed by the Gaia Data Processing and Analysis Consortium (DPAC; <https://www.cosmos.esa.int/web/gaia/dpac/consortium>).

The Guoshoujing Telescope (the Large Sky Area Multi-Object Fiber Spectroscopic Telescope, or LAMOST) is a National Major Scientific Project built by the Chinese Academy of Sciences. Funding for the project has been provided by the National Development and Reform

Commission. LAMOST is operated and managed by the National Astronomical Observatories, Chinese Academy of Sciences.

ORCID iDs

- Xin-Yi Li <https://orcid.org/0000-0003-2086-0684>
 Yang Huang <https://orcid.org/0000-0003-3250-2876>
 Timothy C. Beers <https://orcid.org/0000-0003-4573-6233>
 Hua-Wei Zhang <https://orcid.org/0000-0002-7727-1699>

References

- Baumgardt, H., Hilker, M., Sollima, A., & Bellini, A. 2019, *MNRAS*, **482**, 5138
 Blažko, S. 1907, *AN*, **175**, 325
 Bono, G., Caputo, F., Castellani, V., et al. 2003, *MNRAS*, **344**, 1097
 Catelan, M., & Cortés, C. 2008, *ApJL*, **676**, L135
 Catelan, M., Pritzl, B. J., & Smith, H. A. 2004, *ApJS*, **154**, 633
 Cioni, M. R. L. 2009, *A&A*, **506**, 1137
 Cioni, M. R. L., Habing, H. J., & Israel, F. P. 2000, *A&A*, **358**, L9
 Clement, C. M., Ferance, S., & Simon, N. R. 1993, *ApJ*, **412**, 183
 Clement, C. M., Jankulak, M., & Simon, N. R. 1992, *ApJ*, **395**, 192
 Clementini, G., Ripepi, V., Garofalo, A., et al. 2022, arXiv:2206.06278
 Clementini, G., Ripepi, V., Molinaro, R., et al. 2019, *A&A*, **622**, A60
 Crestani, J., Fabrizio, M., Braga, V. F., et al. 2021, *ApJ*, **908**, 20
 Dambis, A. K., Rastorguev, A. S., & Zabolotskikh, M. V. 2014, *MNRAS*, **439**, 3765
 de Grijs, R., & Bono, G. 2015, *AJ*, **149**, 179
 de Grijs, R., Wicker, J. E., & Bono, G. 2014, *AJ*, **147**, 122
 Deb, S., Singh, H. P., Kumar, S., & Kanbur, S. M. 2015, *MNRAS*, **449**, 2768
 Dékány, I., & Grebel, E. K. 2022, *ApJS*, **261**, 33

- Dékány, I., Grebel, E. K., & Pojmański, G. 2021, *ApJ*, **920**, 33
- Deng, L.-C., Newberg, H. J., Liu, C., et al. 2012, *RAA*, **12**, 735
- Drake, A. J., Catelan, M., & Djorgovski, S. G. 2013a, *ApJ*, **763**, 32
- Drake, A. J., Catelan, M., Djorgovski, S. G., et al. 2013b, *ApJ*, **765**, 154
- Drake, A. J., Graham, M. J., Djorgovski, S. G., et al. 2014, *ApJS*, **213**, 9
- Feast, M. W., Abedigamba, O. P., & Whitelock, P. A. 2010, *MNRAS*, **408**, L76
- Fokin, A. B. 1992, *MNRAS*, **256**, 26
- For, B.-Q., Sneden, C., & Preston, G. W. 2011, *ApJS*, **197**, 29
- Freedman, W. L., Madore, B. F., Scowcroft, V., et al. 2012, *ApJ*, **758**, 24
- Vallenari, A., Brown, A. G. A., et al. 2022, arXiv:2208.00211
- Govea, J., Gomez, T., Preston, G. W., & Sneden, C. 2014, *ApJ*, **782**, 59
- Graczyk, D., Pietrzyński, G., Thompson, I. B., et al. 2020, *ApJ*, **904**, 13
- Hajdu, G., Dékány, I., Catelan, M., Grebel, E. K., & Jurcsik, J. 2018, *ApJ*, **857**, 55
- Harris, W. E. 2010, arXiv:1012.3224
- Holl, B., Audard, M., Nienartowicz, K., et al. 2018, *A&A*, **618**, A30
- Huang, Y., Li, Q., Zhang, H., et al. 2021a, *ApJL*, **907**, L42
- Huang, Y., Yuan, H., Beers, T. C., & Zhang, H. 2021b, *ApJL*, **910**, L5
- Huang, Y., Yuan, H., Li, C., et al. 2021c, *ApJ*, **907**, 68
- Iorio, G., & Belokurov, V. 2019, *MNRAS*, **482**, 3868
- Iorio, G., & Belokurov, V. 2021, *MNRAS*, **502**, 5686
- Jayasinghe, T., Stanek, K. Z., Kochanek, C. S., et al. 2019, *MNRAS*, **486**, 1907
- Jurcsik, J., & Kovacs, G. 1996, *A&A*, **312**, 111
- Kinman, T. D., Cacciari, C., Bragaglia, A., Smart, R., & Spagna, A. 2012, *MNRAS*, **422**, 2116
- Kovacs, G., & Zsoldos, E. 1995, *A&A*, **293**, L57
- Layden, A. C. 1994, *AJ*, **108**, 1016
- Lindegren, L., Bastian, U., Biermann, M., et al. 2021, *A&A*, **649**, A4
- Liu, G., Huang, Y., Bird, S. A., et al. 2022, *MNRAS*, **517**, 2787
- Liu, G. C., Huang, Y., Zhang, H. W., et al. 2020, *ApJS*, **247**, 68
- Liu, X. W., Yuan, H. B., Huo, Z. Y., et al. 2014, in IAU Symp. 298, Setting the Scene for Gaia and LAMOST, ed. S. Feltzing et al. (Cambridge: Cambridge Univ. Press), 310
- Marconi, M., Coppola, G., Bono, G., et al. 2015, *ApJ*, **808**, 50
- Morgan, S. M., Wahl, J. N., & Wieckhorst, R. M. 2007, *MNRAS*, **374**, 1421
- Muhie, T. D., Dambis, A. K., Berdnikov, L. N., Kniazev, A. Y., & Grebel, E. K. 2021, *MNRAS*, **502**, 4074
- Mullen, J. P., Marengo, M., Martínez-Vázquez, C. E., et al. 2021, *ApJ*, **912**, 144
- Mullen, J. P., Marengo, M., Martínez-Vázquez, C. E., et al. 2022, *ApJ*, **931**, 131
- Muraveva, T., Delgado, H. E., Clementini, G., Sarro, L. M., & Garofalo, A. 2018a, *MNRAS*, **481**, 1195
- Muraveva, T., Garofalo, A., Scowcroft, V., et al. 2018b, *MNRAS*, **480**, 4138
- Muraveva, T., Palmer, M., Clementini, G., et al. 2015, *ApJ*, **807**, 127
- Neeley, J. R., Marengo, M., Freedman, W. L., et al. 2019, *MNRAS*, **490**, 4254
- Nemec, J. M., Cohen, J. G., Ripepi, V., et al. 2013, *ApJ*, **773**, 181
- Netzel, H., Smolec, R., Soszyński, I., & Udalski, A. 2018, *MNRAS*, **480**, 1229
- Ngeow, C.-C., Yu, P.-C., Bellm, E., et al. 2016, *ApJS*, **227**, 30
- Pancino, E., Britavskiy, N., Romanó, D., et al. 2015, *MNRAS*, **447**, 2404
- Parisi, M. C., Grocholski, A. J., Geisler, D., Sarajedini, A., & Clariá, J. J. 2009, *AJ*, **138**, 517
- Pietrzyński, G., Graczyk, D., Gallenne, A., et al. 2019, *Natur*, **567**, 200
- Preston, G. W. 1959, *ApJ*, **130**, 507
- Reid, M. J., Menten, K. M., Brunthaler, A., et al. 2014, *ApJ*, **783**, 130
- Ren, F., Chen, X., Zhang, H., et al. 2021, *ApJL*, **911**, L20
- Rimoldini, L., Holl, B., Audard, M., et al. 2019, *A&A*, **625**, A97
- Schlafly, E. F., Finkbeiner, D. P., Schlegel, D. J., et al. 2010, *ApJ*, **725**, 1175
- Schlegel, D. J., Finkbeiner, D. P., & Davis, M. 1998, *ApJ*, **500**, 525
- Scowcroft, V., Freedman, W. L., Madore, B. F., et al. 2016, *ApJ*, **816**, 49
- Sesar, B., Fouesneau, M., Price-Whelan, A. M., et al. 2017a, *ApJ*, **838**, 107
- Sesar, B., Hernitschek, N., Mitrović, S., et al. 2017b, *AJ*, **153**, 204
- Skowron, D. M., Skowron, J., Udalski, A., et al. 2021, *ApJS*, **252**, 23
- Skowron, D. M., Soszyński, I., Udalski, A., et al. 2016, *AcA*, **66**, 269
- Smolec, R. 2005, *AcA*, **55**, 59
- Smolec, R. 2016, in 37th Meeting of the Polish Astronomical Society 3, ed. A. Różańska & M. Bejger (Warszawa: Polish Astronomical Society), 22
- Sollima, A., Cacciari, C., Arkharov, A. A. H., et al. 2008, *MNRAS*, **384**, 1583
- Sollima, A., Cacciari, C., & Valenti, E. 2006, *MNRAS*, **372**, 1675
- Soszyński, I., Udalski, A., Wrona, M., et al. 2019, *AcA*, **69**, 321
- van der Marel, R. P. 2001, *AJ*, **122**, 1827
- van der Marel, R. P., & Cioni, M.-R. L. 2001, *AJ*, **122**, 1807
- Vasiliev, E., & Baumgardt, H. 2021, *MNRAS*, **505**, 5978
- Wagner-Kaiser, R., & Sarajedini, A. 2013, *MNRAS*, **431**, 1565
- Wang, C., Yuan, H., & Huang, Y. 2022a, *AJ*, **163**, 149
- Wang, F., Zhang, H. W., Xue, X. X., et al. 2022b, *MNRAS*, **513**, 1958
- Wang, F., Zhang, H. W., & Xue, X. X. 2023, in press
- Weinberg, M. D., & Nikolaev, S. 2001, *ApJ*, **548**, 712
- Yang, L., Yuan, H., Zhang, R., et al. 2021, *ApJL*, **908**, L24
- Yanny, B., Rockosi, C., Newberg, H. J., et al. 2009, *AJ*, **137**, 4377
- Yuan, H. B., Liu, X. W., & Xiang, M. S. 2013, *MNRAS*, **430**, 2188
- Zhao, G., Zhao, Y.-H., Chu, Y.-Q., Jing, Y.-P., & Deng, L.-C. 2012, *RAA*, **12**, 723
- Zinn, J. C. 2021, *AJ*, **161**, 214